6
Nuclear Magnetic Resonance Studies of Zeolites

Clare P. Grey
State University of New York at Stony Brook, Stony Brook, New York, U.S.A.

I. INTRODUCTION

Nuclear magnetic resonance (NMR) has been widely used to characterize zeolite structure, acidity, and binding sites, and to study catalytic reactions or sorption processes that occur within the pores of zeolites. NMR is a probe of local structure and often serves as a complementary tool for the probe of long-range order, namely, diffraction. The NMR spectra are sensitive to a range of local interactions, which provide detailed spatial and chemical information. Furthermore, NMR spectroscopy is a *quantitative* probe of the *whole* sample and, thus, can be used or to follow the fate of molecules inside the pores of the zeolite, during a catalytic reaction or following gas sorption, or to determine, for example, the extent of aluminum substitution into the zeolite framework. The time scale of the interactions probed by NMR spectroscopy can be close to the time scale of many motional processes, and so NMR can be used to study the dynamics of molecules sorbed in the pores of the zeolites or to study longer range diffusional processes (see Chapter 10).

More than 3500 papers involving the application of NMR spectroscopy to the study of zeolites were published in or before 1993, and by the end of 2001 the number had risen to over 6000. The field was reviewed by Fyfe *et al.* in 1991 (1) and by Klinowski in 1993 (2). Thus, this chapter will focus primarily on some of the more recent uses of NMR, which make use of some of the newer NMR methodology developed during the last 10 years. However, the routine use of, for example, ^{29}Si magic angle spinning (MAS) NMR to determine aluminum framework content or to count the number of crystallographic sites in purely siliceous materials, and ^{27}Al MAS NMR to investigate the framework and extraframework species, still remain the most widely applied NMR methods. Therefore, these methods will also be discussed briefly.

This chapter is not intended as a review of the entire subject but rather as an introduction to the use of the method to study zeolites and as an outline of some of the applications of NMR spectroscopy in this field. Examples are provided to illustrate how NMR can be used to tackle different problems or research projects, along with a brief description of the theory of some of the experiments. This chapter will focus primarily on zeolite structural characterization and on the characterization of binding sites in the zeolite channels or pores. Applications of particular experiments to other molecular sieves, such as aluminum phosphates (or $AlPO_4$s), are mentioned only briefly. The applications of NMR to study catalytic processes or of solution NMR methods

Table 1 Summary of Some of NMR Approaches Used to Study Zeolites[a]

Method	Application	Ref.
	General Characterization of Zeolite Structures	
^{29}Si MAS	Quantification of aluminum content or nature of the heteroatom substituted in the framework Estimation of Si-O-Si bond angles Quantifying the number of crystallographic sites and identification of space group or symmetry Measure of crystallinity	
^{27}Al MAS	Identification of extraframework aluminum oxide species Determination of coordination number for Al in molecular sieves (e.g., $ALPO_4$s) Dealumination and realumination of frameworks Characterization of Lewis acid sites	
^{1}H MAS	Characterization and quantification of Brønsted acid sites Investigation of reactivity of molecules in the zeolite pores	
^{13}C MAS	Catalytic studies of reactivity (both in situ and ex situ) and of the intermediates formed during a reaction Combination with *ab initio* studies of ^{13}C chemical shifts	179
^{2}H	Investigation of mobility of sorbed molecules Characterization of Brønsted acid sites	215–217 52
^{27}Al, ^{31}P, ^{19}F, ^{14}N	In-situ NMR studies of zeolite synthesis under hydrothermal conditions In situ measurement of pH during zeolite synthesis	218 219
^{14}N	Characterization of interactions between the templates and fragments of the zeolite framework formed during synthesis	
^{23}Na MAS, MQMAS and DOR	Characterization of number and locations of Na^+ cations in fully and partially exchanged sodium zeolites Identification of the cation sites involved in binding Changes in cation occupancies on gas sorption and temperature	
^{23}Na, ^{29}Si, ^{27}Al ^{133}Cs MAS	Characterization of alkali metal clusters in zeolite cages Characterization of Cs^+ positions as a function of Cs^+ exchange level and dehydration temperature Determination of the cation sites available for binding Characterization of superbasic sites	220–225
^{19}F MAS	Characterization of fluoride ions in highly siliceous zeolites Identification of five-coordinate silicon Characterization of fluoride species following reaction with fluorine-containing gases	
^{17}O MAS, DOR, and MQMAS	Characterization of framework oxygen sites in siliceous zeolites or zeolites where Si/Al = 1 Separation of the Si-O-Si and Si-O-Al oxygen sites	

(*Continued on next page*)

Table 1 *Continued*

Method	Application	Ref.
$^{11}B/^{10}B$, ^{51}V, $^{6}Li/^{7}Li$, ^{71}Ga	Characterization of heteroatom substitution in zeolite frameworks	
^{207}Pb, ^{113}Cd, (^{1}H)	Characterization of extraframework cations and cation exchange reactions (Ag^{+}, Cd^{2+}, Pb^{2+}, Ca^{2+})	94,226,227
^{129}Xe	Characterization of pore sizes and shapes, and cation distributions	228–230
Sorption of O_2	Identification of lithium, sodium, cesium, and proton sites available for gas binding (in combination with ^{6}Li, ^{7}Li, ^{23}Na, ^{133}Cs, or ^{1}H NMR)	121,126
	Double-Resonance and Two-Dimensional Correlation Experiments	
$^{27}Al/^{31}P$	Assignments of resonances due to framework sites in $AlPO_4$'s and investigation of their connectivity to different Al/P sites (from SEDOR, TRAPDOR and REAPDOR experiments) Identification of Lewis and Brønsted acid sites in zeolites, by using phosphorus-containing probe molecules (TRAPDOR) Investigation of coordination number of Lewis acid sites (INEPT)	
$^{1}H/^{27}Al$	Indirect detection of Brønsted acid sites Assignment of ^{1}H resonances Characterization of extraframework sites (TRAPDOR and REAPDOR) Measurement of H-Al distances (SEDOR)	
$^{27}Al/^{15}N$ and $^{27}Al/^{14}N$	Identification and quantification of Brønsted and Lewis acid sites (REDOR and TRAPDOR) Measurement of Al-N distances to characterize binding of basic probe molecules (REDOR)	
$^{23}Na/^{29}Si$	Characterization of the location of Na^{+} cations (REAPDOR)	
^{29}Si	Connectivity of different framework sites, by using (COSY and INADEQUATE two-dimensional experiments)	
$^{1}H/^{29}Si$	Location of molecules in the channels of highly siliceous zeolites (CP) Characterization of template/zeolite precursor interactions during the synthesis of siliceous ZSM-5 (CP)	231,232
$^{13}C/^{27}Al$	Characterization of probe molecule/zeolite interactions (TRAPDOR, REDOR, and REAPDOR)	233
$^{1}H/^{13}C$	Binding of (deuterated) carbon-containing template molecules to protonated defect sites (REDOR, CP)	

[a]The pulse sequences used in the experiments are given, where relevant, in parentheses. References are provided for topics that will not be covered in Secs. II–IV or will only be discussed very briefly.

to follow the zeolite nucleation and growth reactions that occur during zeolite synthesis are largely outside the scope of this chapter. For completeness, however, some examples in this area are documented in Table 1 and some of the challenges are discussed in Sec. III.

This chapter will be presented as follows: We first present a summary of some recent uses of zeolites in the form of a table. Many of these applications are then outlined in Sec. II. A more detailed but by no means comprehensive description of the NMR experiments, along with some specific examples of variants of particular sequences that have been applied to zeolites, is provided in the theory section presented at the end of the chapter (Sec. IV). The aim of Sec. IV is to provide the reader with a brief background to some of the principles behind the experiments and an explanation of some of the terms routinely used in NMR. This section attempts to address the large disconnect between the detailed NMR papers that describe the theory behind the NMR experiments and the more qualitative descriptions of these experiments, often provided in papers written for the zeolite community. We assume that the reader is familiar with the basics of solid-state NMR and terms such as magic angle spinning (MAS), and 90° (or $\pi/2$) pulses. The section on 1/2-integer spin quadrupolar nuclei is somewhat more detailed, since these nuclei are widely found in zeolites; the acquisition of NMR spectra from these systems can sometimes be nontrivial and, more importantly, can often be misleading. Thus, we have attempted to outline some of the pitfalls and solutions to some of the problems. The sections are written, insofar as is possible, so that Secs. II and III are still approachable for a reader who is less interested in the underlying NMR theory.

II. APPLICATIONS OF NMR SPECTROSCOPY TO STUDY ZEOLITE STRUCTURE

A. ^{29}Si MAS NMR Studies

1. Aluminum Substitution and Framework Structure

In as early as 1980, Lippmaa, Engelhardt, and coworkers showed that the ^{29}Si MAS NMR of aluminum-containing zeolites contain well-resolved ^{29}Si resonances whose shift depend on the number of aluminum atoms in the silicon local coordination sphere $Si(OSi)_{4-x}(OAl)_x$ (3,4). The introduction of each aluminum atom into the silicon coordination sphere results in a shift of approximately 5–6 ppm from the typical chemical shift position of a $Si(OSi)_4$ local environment at approximately −102 to −110 ppm. Typically, up to five resonances can be observed corresponding to $x = 0$, 1, 2, 3, and 4 (Fig. 1). The intensity of the resonances can be used to quantify the concentration of each local environment and then determine the amount of aluminum substituted into the framework, and thus the Si/Al ratio (5–7). Since the substitution of aluminum in zeolite frameworks is not random and "Loewenstein's rule" is generally observed (i.e., no Al-O-Al linkages are formed in the framework), this needs to be taken into account when calculating the Si/Al ratio:

$$\mathrm{Si/Al} = \sum_{x=0}^{4} I_{\mathrm{Si(OAl)}_x} \Big/ \sum_{x=0}^{4} 0.25 \times I_{\mathrm{Si(OAl)}_x} \tag{1}$$

The total silicon concentration is proportional to the total intensity of all five potential resonances in the ^{29}Si spectrum (i.e., $\sum_{x=0}^{4} I_{\mathrm{Si(OAl)}x}$, where $Si(OAl)_x$ represents the local environment $Si(OSi)_{4-x}(OAl)_x$). The total aluminum content is proportional to the weighted sum of the intensities of all the resonances due the environments $Si(OSi)_{4-x}(OAl)_x$, where the intensity of each resonance is weighted by the number of aluminum atoms in the local environment. The

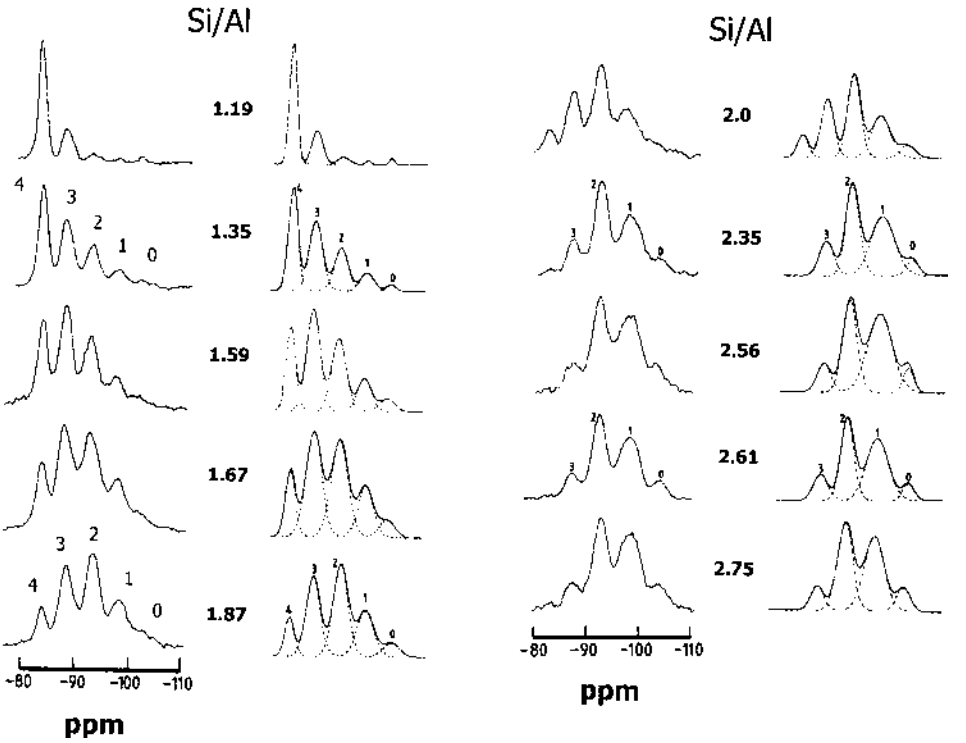

Fig. 1 The ^{29}Si MAS NMR experimental and simulated spectra of zeolites NaX and NaY showing the five different resonances from the local environments $Si(OSi)_{4-x}(OAl)_x$, $x = 0$–4. Values of x are marked above the resonances. (Reproduced from Ref. 214.)

sum must then be divided by 4 to account for the fact that each silicon atom is connected to four other silicon or aluminum atoms. The aluminum framework content determined by this method is more accurate than that determined by analytical (ICP) methods for the whole sample, since the latter method cannot distinguish between framework and extraframework aluminum. The presence of extraframework aluminum species can be confirmed by ^{27}Al NMR (see Sec. II.B). Note also that the isoelectronic Si^{4+} and Al^{3+} ions cannot be distinguished by X-ray diffraction.

The silicon shift has been correlated with the mean Si-O-Si bond angle, θ (8–11), the bond angle controlling the s/p character of the oxygen orbitals used to bind to the two adjacent silicon atoms (12). This observation can be used to assign the different resonances if the structure is known or, conversely, provide structural information for an unknown structural type. A series of correlations have been developed by plotting the shift, δ, vs. θ, sin(θ/2), and cos θ/(cos θ−1), all these approaches providing reasonable correlations, primarily because all of these angular functions are close to being linear over the angular ranges typically exhibited by the materials that have been investigated. Ramdas and Klinowski proposed a general relationship (13):

$$\delta/\text{ppm} = 143.03 + 7.95n - 20.34vd_{\text{TT}} \tag{2}$$

where n is the number of aluminum atoms in the silicon local coordination sphere and vd_{TT} is the sum of the four average Si-T distances (T indicates a tetrahedrally coordinated atom such as

Si or Al) around the central Si atom, assuming Si-O and Al-O bond lengths of 1.62 and 1.75 Å, respectively, and is defined as:

$$vd_{TT}/\text{Å} = [3.37n + 3.24(4 - n)]\sin(\theta/2) \quad (3)$$

The effect of aluminum substitution on the shift is included in the expression via the "7.95*n*" term.

The use of *ab initio* calculations to calculate chemical shifts directly from the crystallographic structure is starting to become more routine (14–17). The level of accuracy that can be obtained by these methods is steadily increasing, in part due to increased computer power and the consequent ability to study larger zeolite fragments or unit cells and to use higher level basis sets to describe the atomic orbitals. It is extremely likely that this approach will become more widely used to help assign resonances and to optimize, or to provide a check on, the bond angles obtained from diffraction experiments (14).

2. Dealumination Studies

Silicon NMR can be used to monitor dealumination, since changes in the Si/Al ratio can be detected (18) along with the formation of defects in the form of silanols (2). Silanols can be formed via reactions involving the destruction of the framework of the form:

$$\text{Si-O(H)-Al} + \text{H}_2\text{O} \rightarrow \text{Si-OH} + \text{HO-Al}$$

which can occur during dehydration or steaming. Substitution of one -O-Si linkage by an -OH group (converting a so-called Q^4 group to a Q^3 group) results in a shift of the ^{29}Si resonance by approximately +10 ppm. Thus, resonances with local environments $Si(OAl)_x(OSi)_{4-x}$ and $Si(OH)(OAl)_y(OSi)_{3-y}$ where $x = y + 1$ [i.e., $Si(OAl)(OSi)_3$ and $Si(OH)(OSi)_3$, when $y = 0$] often overlap; this can lead to errors in the determination of the Si/Al ratio. The ^{1}H/^{29}Si cross-polarization (CP) double-resonance experiment can be used to select for ^{29}Si nuclei that are nearby protons, particularly if short contact times are used (Fig. 2). Although this experiment is not quantitative unless a series of calibration experiments are performed, CP can be used to

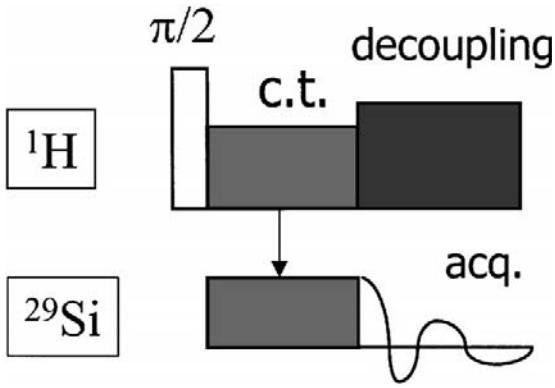

Fig. 2 The ^{1}H to ^{29}Si cross-polarization NMR experiment used to select for silicon atoms that are nearby protons. The distance over which the ^{1}H magnetization is transferred may be controlled by varying the contact time (c.t.). Shorter values of the c.t. are used to select for protons nearby silicon. ^{1}H decoupling may be applied, if required, during the acquisition of the ^{29}Si free induction decay (FID).

identify the silanol defect species and to determine whether they are present in large concentrations and, thus, need to be taken into account when determining the Si/Al ratio. For example, two $Si(OH)(OSi)_{3-y}(OAl)_y$, $y = 0$ and 1, groups were observed with $^1H/^{29}Si$ CP in a mildly dealuminated faujasite. The presence of an aluminum atom in the silicon local coordination sphere for the $x = 1$ group was confirmed with a $^{29}Si/^{27}Al$ double-resonance NMR experiment (19).

3. Highly Siliceous Zeolites

Fyfe and coworkers showed that the resolution observed in the ^{29}Si spectra of zeolites could be dramatically improved by studying extremely crystalline samples of highly siliceous zeolites (1). The materials were synthesized directly, obtained chemically via treatment of samples with $SiCl_4$ and water vapor, or subjected to hydrothermal treatment. The broadening due to aluminum is associated with the local disorder in the lattice (i.e., small variations in bond angles and bond lengths) caused by framework substitution and interactions with the extra-framework cations or protons. Perhaps some of the most classic applications of this approach can be found in the ^{29}Si MAS NMR of MFI and related zeolites. Analysis of the ^{29}Si of highly siliceous ZSM-5 (Sil-ZSM-5) showed that there were 25 independent, crystallographically distinct silicon atoms (or T atoms) in the unit cell (20,21); the result confirmed that this material adopts a monoclinic space group. ^{29}Si could then be used to follow the monoclinic to orthorhombic phase transition that occurred on sorption of some organics such as paraxylene (22). The approach has been used to study the phase transitions that occur with other gases such as pyridine and on heating of the sample (21).

Fyfe et al. used two-dimensional COSY and INADEQUATE experiments to probe longer range structure (1,23–28). Both of these NMR experiments exploit the J coupling between the silicon nuclei of the zeolite framework and thus can be used to study the connectivities between different framework sites. Initial experiments were performed on ^{29}Si-enriched samples of ZSM-39 by using a $^1H \rightarrow {}^{29}Si$ CP experiment to enhance the signal of the silicon atoms ^1H spin lattice relaxation times (T_1's) are 3s in comparison to the ^{29}Si T_1's of 650s (29). Once the size of the J couplings had been established, experiments on nonenriched samples became feasible (24). These experiments have been reviewed in detail in Ref. 1.

Koller et al. have investigated the effect of synthesizing high-silica zeolites (beta, SSX-23, ITQ-3, ZSM-12, silicalite) in the presence of fluoride ions as mineralizing agents (30). The fluoride ions serve to charge balance the templating agents (protonated amines) and prevent theformation of significant concentrations of defects. The ions are actually incorporated into the framework, to form SiO_4F^- units. The ^{29}Si shift for this five-coordinated environment for silicon was found to lie between -140 and -150 ppm. ^{19}F MAS NMR studies showed that the fluoride ions were mobile at ambient temperatures in some of the systems studied. For example, in silicalite, the sample had to be cooled to 140 K before the fluoride ion motion was frozen out, on the ^{19}F chemical shift time scale. The ^{29}Si NMR spectra for the mobile systems contain much broader resonances with shifts between -120 and -150 ppm. This is consistent with rapid exchange between four- and five-coordinate silicon, caused by the fluoride ion motion.

Highly siliceous zeolites synthesized in the absence of fluorine contain defects in the framework to charge compensate for the cations used as templating agents. These defects take the form of $Si\text{-}O^-$ groups (i.e., nonprotonated silanol groups). The interactions between these groups and the templating agents have been studied in detailed by Shantz and Lobo, by using $^1H/^2H$ CP and heteronuclear correlation (HETCOR) NMR experiments (31–33). The formation of the defect can involve the loss of a silicon atom from the framework, with the loss of a central silicon atom in the $Si(\text{-}O\text{-}Si)_4$ local environment resulting in four $Si\text{-}O^-$ species. The

Si-O$^-$ oxide ions are basic and may be readily protonated forming a hydroxyl nest comprising, in theory, up to four framework SiOH groups:

$$(\text{Si-O}_{\text{fram}^-})_4\text{Si} + 4\text{H}_2\text{O} \rightarrow 4\ (\text{Si-O}_{\text{fram}^-})_3\text{Si-OH} + \text{Si(OH)}_4$$

Double-quantum and triple-quantum two-dimensional ^{1}H MAS NMR spectroscopies were used to show that the defect formed in Sil-ZSM-12 synthesized with deuterated benzyltrimethylammonium cations consists of a charge compensating Si-O$^-$ group, hydrogen bonded to *three* Si-OH groups in the defect or hydroxyl nest (34). Average distances between the protons of 3.1 ($\pm$0.1Å) were obtained, assuming that the protons are rigid at room temperature. The Si-O$^-$ group is strongly hydrogen bonded to the nearby Si-OH groups, resulting in a very large ^{1}H shift for the silanols of 10.2 ppm (34). A ^{1}H to ^{2}H HETCOR experiment was used to show that the proton(s) in this defect site are located close to the structure-directing agents (SDAs). For example, Fig. 3 shows a ^{1}H to ^{2}H HETCOR experiment for nonasil synthesized in the presence of the partially deuterated SDA *N,N,N*-trimethylcyclopentylammonium-d_9 hydroxide. A cross-peak is observed between the protons of the silanol defect (10.2 ppm) and the deuterated methyl groups of the SDA, indicating that the methyl groups are in proximity to the defect.

4. ^{29}Si NMR Studies of Heteroatom Substitutions in Frameworks Other Than Al

^{29}Si NMR has now been shown to be sensitive to the substitution of a range of other heteroatoms or T atoms into the framework, and can often be used to prove that these ions have been substituted. This is sometimes difficult to show conclusively by diffraction methods. Even the observation of a short Si-M distance in an extended X-ray absorption fine structure (EXAFS) experiment, where M is the heteroatom, does not definitely prove that the heteroatom is incorporated into the framework: short Si-M distances can often be observed between framework and extraframework cations.

Examples where the ^{29}Si chemical shift is significantly shifted by substitution of T atoms into the Si local coordination sphere include T = Li in lithosilicates (35,36), T = Ga in gallosilicates (37), and T = Zn in zincosilicates (38,39). The effect of cation substitution on the ^{29}Si MAS NMR spectra has been studied in detail by Weller et al. for Ge, Ga, Al, and Be substitution of a series of sodalites (40). Shifts of 3.2 ppm from Si(OAl)$_4$ to Si(OGa)$_4$ for the same T-O-T angle were observed (i.e., O-Ga for O-Si substitution results in a shift of about 6 ppm), while even larger shifts were observed for Be substitution, e.g., the ^{29}Si resonance for the Si(OBe)$_4$ local environment in beryllium silicon sodalites lie between $-$67.8 and $-$74 ppm depending on the nature of the cation and anions in the sodalite cages. These authors also established correlations between ^{27}Al, ^{71}Ga shifts and the T-O-T′ bond angles. A similar ^{29}Si shift of 6.7 ppm for gallium substitution for Si in six different topologies (ABW, SOD, FAU, LTL, MAZ, and CGS) was determined by Cho et al. (37).

Unfortunately, there are a series of heteroatoms whose substitution does not appear to be associated with a very large shift (i.e., the changes in ^{29}Si chemical shift are smaller than or comparable to the distributions of chemical shifts for the different crystallographic sites found in the purely siliceous materials). Examples of systems that fall into this category include vanadium-, boron-, and titanium-substituted zeolites (41–44). Fortunately, many of these heteroatoms are NMR active, providing an alternative approach for probing their local environments in the framework (see II.C).

B. ^{27}Al Studies of Framework and Extraframework Sites

^{27}Al MAS NMR spectroscopy has been widely used to study aluminum substitution in zeolites (45). ^{27}Al is a spin-5/2 quadrupolar nucleus with a moderately large quadrupole moment. This

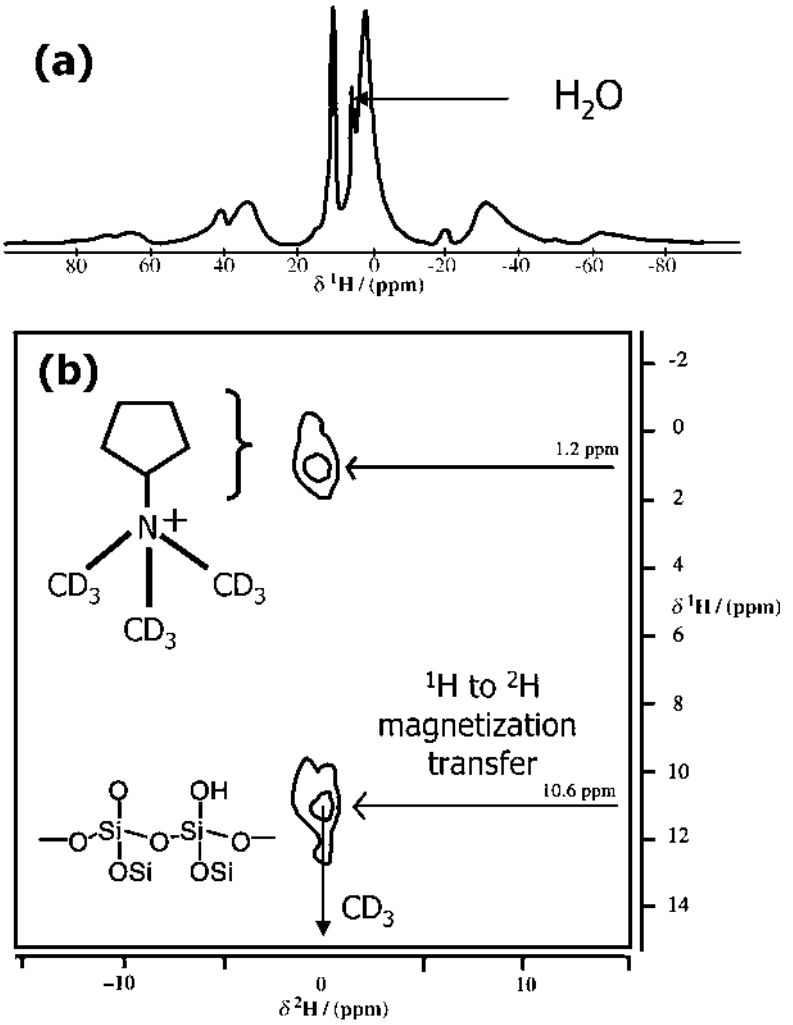

Fig. 3 (a) The ^{1}H MAS NMR spectrum and (b) two-dimensional ^{1}H to ^{2}H HETCOR NMR spectrum of nonasil synthesized by using *N,N,N*-trimethylcyclopentylammonium-d_9 hydroxide as the SDA. A cross-polarization sequence, with a contact time of 300 μs, was used to transfer ^{1}H magnetization to the ^{2}H spins (which were then detected) in the HETCOR experiment. (Adapted from Ref. 54.)

has important implications, particularly for characterizing the dehydrated, acidic forms of many zeolites, which tend to contain highly distorted aluminum local environments. Distorted local environments are typically associated with large electric field gradients (EFGs), and thus large quadrupole coupling constants (QCCs). This has two important implications of which the reader must be aware: (a) Not all ^{27}Al signals may be detected, particularly if "standard," one-pulse NMR methods are used at lower fields. (b) The isotropic shift of the resonance is a sum of the chemical shift *and* the quadrupole-induced shift. For environments with large QCCs, and at low magnetic fields strengths, the latter contribution may be large and must be estimated (e.g., by running the spectra at different field strengths or by measuring the QCC) before an accurate value of the chemical shift can be extracted. The implications, potential pitfalls, and solutions are discussed in considerable detail in the theory section.

^{27}Al spectra show distinct chemical shift ranges for tetrahedral, pentacoordinate, and octahedral environments, and so can be used to distinguish between aluminum framework and extraframework species. Aluminum tetrahedral framework atoms typically resonate at 60–50 ppm, and can be clearly distinguished from five- and six-coordinate extraframework species at approximately 25 and 13 to −17 ppm, respectively (45). The highly symmetrical four-coordinate AlO_4^{5-} anion that is sometimes formed in the sodalite cages of X and Y zeolites following mild dealumination or calcination resonates at a higher frequency of 70–90 ppm and can, therefore, be easily resolved (Fig. 4) (46,47).

The quadrupole coupling constants for the hydrated, cation-exchanged forms of zeolites are typically moderately small (0.6–2 MHz) (45), and spectra are readily acquired from these materials. The QCCs increase noticeably on dehydration, as the water molecules that hydrogen bond to the framework and bind to the cations are removed. Broad resonances are observed with shoulders (or tails) to lower frequencies (Fig. 4a). These lineshapes are characteristic of a distribution of QCCs, due to the range of local environments that occur in these materials. In general, the QCC of a zeolite increases as the charge on the extraframework cation increases, which is presumably a consequence of the lower numbers of cations coordinated to the nearby oxygen atoms *and* the higher charge on the cations. Two-dimensional multiple-quantum MAS (MQMAS) methods (48,49) have now been applied to the study of zeolites and aluminophosphates ($AlPO_4$'s), with the method allowing the different crystallographic sites for aluminum in many $AlPO_4$'s to be resolved (50,51).

The dehydrated proton forms are associated with very large QCCs of more than 13–16 MHz (52). To a first approximation, this is a consequence of the large differences in charge between the one protonated oxygen and the three other nonprotonated oxygen atoms

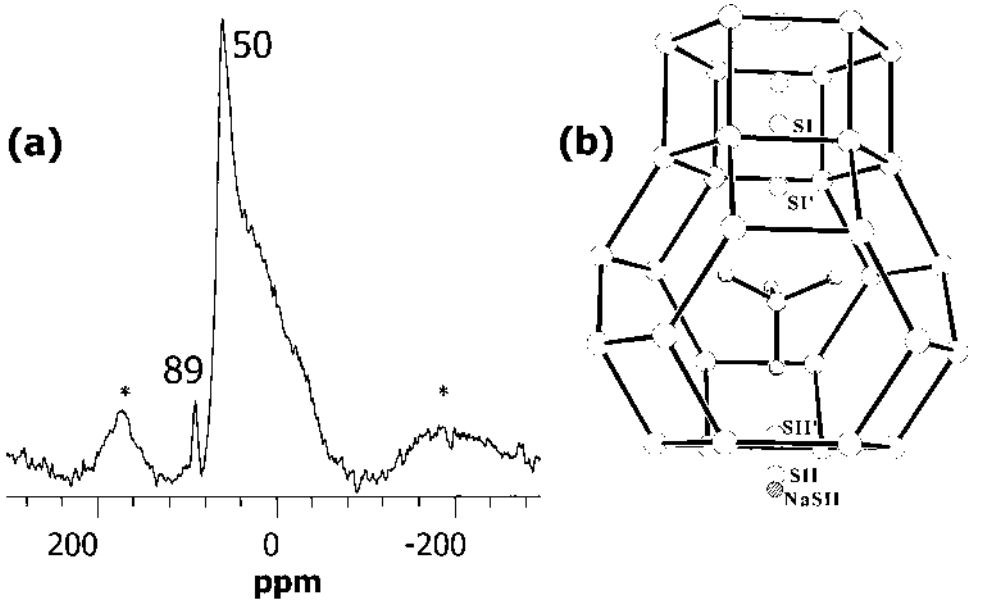

Fig. 4 (a) The ^{27}Al MAS NMR spectrum of dehydrated Zn^{2+}-exchanged NaY, collected at a field strength of 8.4 MHz, showing the resonance due to the extraframework AlO_4^{5-} species, and the broadening of the resonance due to the tetrahedrally coordinated framework aluminum atoms. (Spinning speed = 10 kHz; asterisks denote spinning sidebands). (b) The location of the AlO_4^{5-} species and cations obtained from X-ray diffraction. (Adapted from work published in Ref. 68.)

coordinated to the central aluminum atom in this Al(-O-Si)$_3$(-O(H)-Si) local environment (53). These local environments are difficult to observe by one-pulse MAS methods, since the broadening caused by the second-order quadrupolar interaction is larger than the spinning speed, and broad featureless resonances are observed, which are difficult to distinguish from the baseline. These aluminum spins are often termed "invisible," but they can be observed in a "wideline" spectrum by using a spin echo. Ernst et al. were able to detect the ^{27}Al central transition of various dehydrated H zeolites under nonspinning conditions and to extract a value of, for example, 16 MHz for the QCC for dehydrated H-ZSM-5 (52).

An alternative approach to detect the invisible spins is to use the TRAPDOR (TRAnsfer of Populations in DOuble Resonance) NMR method (54,55). The experiment has been used to determine the ^{27}Al quadrupole coupling constants of different "invisible" aluminum environments in steamed and unsteamed zeolites, and to characterize the aluminum Lewis and Brønsted acid sites (55–57). These environments have now been directly observed in MQMAS methods, by using a combination of very high field strengths and very large spinning speeds. The Al-O(H)-Si resonance, more importantly, could be *separated* from extraframework environments that are either partially rehydrated or coordinated to extraframework cations, such as Na^+, which remain due to incomplete ion-exchange processes (58).

^{27}Al has been used extensively to study the extraframework aluminum species formed during synthesis, ion exchange, calcination, or following chemical modification (2). Interest in this area stems in part from the Lewis acidity is associated with these species, and the possible interaction between the extraframework aluminum oxide/hydroxide clusters and the remaining Brønsted acid sites. Care is required before the concentration of these species can be determined from the ^{27}Al MAS NMR spectra (see Sec. IV), even when the samples are fully hydrated. Four-, five-, and six-coordinate extraframework species may be present, giving rise to overlapping resonances in the one-pulse ^{27}Al MAS spectra. Nonetheless, these spectra typically show very characteristic features and peaks that have been assigned to five- and six-fold coordinated species, allowing different local environments to be identified. High-field ^{27}Al MQMAS NMR experiments have recently been used to separate the resonances due to two four-coordinate aluminum species in ultrastable Y (US-Y) (59). MQMAS studies of steamed and acid-washed faujasite zeolites, performed at moderate field strengths (9.4 T) have suggested that the ^{27}Al resonance at approximately 32 ppm, which is often assigned to five-coordinated Al, is due to a distorted four-coordinated site (60). Fields corresponding to ^{1}H frequencies of 600 and 800 MHz were used in the former study (59), and it is clear that the use of steadily higher fields in this research area will make such experiments increasingly more routine and yield fewer ambiguous results. Furthermore, simple one-pulse experiments will also yield spectra with higher resolution at these high fields, and the concentrations of the different species will become more straightforward to extract.

C. Heteronuclear NMR Studies of Heteroatom Substitution in Frameworks

The nuclei that have been most extensively studied include boron (^{10}B and ^{11}B), gallium (^{71}Ga), and vanadium (^{51}V) (61,62). ^{49}Ti has been used to study a number of titanates (63,64), but the ($I = 5/2$) nucleus has a large quadrupole moment, which results in extremely broad resonances for distorted local environments. The Ti site in zeolites is typically invisible, but extremely high field strengths may make these experiments more feasible.

1. Boron

Although boron substitution does not appear to result in a significant shift in the ^{29}Si resonance, following substitution in the framework, both ^{11}B and ^{10}B are amenable to NMR studies

(61,62,65–69). The as-synthesized zeolites contain four-coordinate BO_4^{5-} groups. These groups show a characteristic sharp ^{11}B resonance due to the relatively symmetrical environment for boron. Calcination to remove the templating agent and dry these materials appears to result in the formation of trigonal boron groups (BO_3^{3-}) via reactions of the form:

$$\text{Si-O(H)-B(OSi)}_3 \rightarrow \text{Si-OH} + \text{B(OSi)}_3$$

This reaction is accompanied by the growth of a broader ^{11}B resonance, shifted to higher frequencies, with a characteristic second-order quadrupolar lineshape due to the more distorted trigonal environment. The boron is readily removed from the framework.

2. Gallium

^{71}Ga has been used to study gallium substitution in zeolites and gallophosphate molecular sieves, and resonances due to tetrahedrally coordinated gallium (with similar lineshapes to those seen for aluminum framework sites in ^{27}Al spectra) have been observed (70,71). In the case of a gallosilicate with the NAT topology, a lineshape dominated by the second-order quadrupolar interaction was seen. This was ascribed to an unusual degree of local order due to a nonrandom distribution of Si and Ga in the framework (37).

3. Lithium

Both ^6Li and ^7Li have been used to investigate lithium substitution in lithosilicates (36); although the ^6Li ($I = 1$) nucleus has a lower natural abundance, higher resolution spectra can be obtained with ^6Li in comparison with ^7Li. The application of this method is hampered by the very small chemical shift range of lithium, and sometimes by the rapid exchange of the lithium between the different framework and extraframework sites. However, recent studies have shown, that the resolution is significantly improved if the ^6Li spectra are acquired at higher fields, allowing framework and extraframework sites to be distinguished (72).

4. Vanadium

Vanadium substitution in zeolites has been studied by using the $I = 5/2$ ^{51}V isotope. Although a quadrupolar nucleus, ^{51}V has a very small quadrupole moment; thus, only small or negligible broadening of the central transition is observed. The second-order quadrupolar-induced contribution to the shift may be found by extracting the ^{51}V isotropic resonance as a function of the field strength. Vanadium environments are typically extremely distorted and, hence, the ^{51}V NMR resonances typically show large chemical shift anisotropies (CSAs). The relationships between ^{51}V chemical shifts, CSAs, and local coordination environments have been studied in some detail, in part due to the role that many vanadates play in catalysis (73). Although correlations have been established, the shifts for four-, five-, and six-coordinate vanadium environments do not show well-separated chemical shift ranges.

A detailed electron spin resonance (ESR) and NMR study of V-substituted ZSM-12 has been reported (41). A ^{51}V resonance (at -610 ppm) could only be detected in the calcined sample, with a quadrupole coupling constant that is consistent with a distorted coordination environment such as $_3$(Si-O-)V=0, where the vanadium atom is coordinated to three framework oxygen atoms. Silanol groups were observed by ^{29}Si NMR, consistent with the presence of this vanadium species. No signal was observed for the as-synthesized materials. ESR of the as-synthesized samples revealed the presence of a vanadium environment due to the paramagnetic V(IV) species VO^{2+}. A second V(IV) tetrahedral species was also postulated to be present, which could not be detected by either ESR or NMR. ^{51}V NMR studies of a wider range of

zeolites have suggested that other species may be present, which depend on the synthesis method and the level of hydration of the zeolites (74,75).

D. ^{17}O MAS NMR Studies of Oxygen Framework Sites

The $I = 5/2$ quadrupolar ^{17}O nucleus may be used to probe the local environment of oxygen in a zeolite framework. This nucleus is extremely sensitive to its local coordination environment (with a chemical shift range of >1000 ppm), large chemical shift differences being observed as a function of the Si-O-Al environment, and between Si-O-Si and Si-O-Al environments (76–78). Enriched samples are generally required, a factor that has limited the number of studies in this field to date. A number of studies have shown that ^{17}O can be readily introduced into the framework by heating the zeolites at 500–750°C in $^{17}O_2$ gas. For example, Sil (siliceous)-FER was exchanged by heating the sample for 18 h at 750°C in $^{17}O_2$ (14). Lower temperatures may be used for aluminum-containing zeolites (79). An alternative approach involves steaming the zeolites in $H_2{}^{17}O$ at approximately 250°C (77). Stebbins et al. have studied the kinetics of oxygen exchange with $H_2{}^{17}O$ between 157°C and 197°C for the natural zeolite stilbite and have shown that the Si-O-Al oxygen atoms are exchanged more rapidly (80). For example, approximately 30% of the Si-O-Si and 60% of Si-O-Al sites were exchanged, following reaction in $H_2{}^{17}O$ at 197°C for 80 h. However, both approaches appear to lead to some exchange of *all* the oxygen sites, provided the exchange is performed for sufficiently long time. The preferred method will depend on the stability of the particular zeolite under investigation under steaming vs. high-temperature conditions.

The ^{17}O nucleus has a large quadrupole moment, and the one-pulse spectra of this nucleus are typically very broad, consisting of a large number of overlapping resonances. This is a particular problem for aluminum-containing zeolites that do not contain strictly alternating Si and Al atoms (i.e., when both Si-O-Al and Si-O-Si oxygen atoms are present). Double rotation (DOR) (81,82), dynamic angle spinning (DAS) (83), and MQMAS have been used to obtain high-resolution ^{17}O spectra for zeolites with Si/Al ratios of one, in which the individual resonances due to the different crystallographic sites may often be resolved (76,77). The purely siliceous materials also yield high-resolution spectra because only Si-O-Si linkages are present.

One challenge in this field lies in correctly assigning the observed signals to the different crystallographic sites. The ^{17}O QCCs of the Si-O-Si and Si-O-Al groups are very different and strongly depend on the nature of the nearest-neighbor (Si or Al) atoms (76). Smaller QCCs (of approximately 3.2–3.6 MHz for the sodium-exchanged zeolites) are generally seen for Si-O-Al groups (76,77), whereas larger QCCs of more than 5 MHz are seen for Si-O-Si groups (14,78). There is a weak correlation between the QCC and the Si-O-Si bond angles in the siliceous materials, with the QCC increasing from approximately 5.1 MHz to 5.6 MHz as the angle increases from 137° to 167°. However, QCCs of 5.6 and 5.4 MHz were obtained for sites in ferrierite and faujasite with Si-O-Si bond angles of 165° and 167°, respectively (14). The results indicate that the correlation is not strong enough to allow the resonances to be assigned based solely on the bond angle. These results are consistent with Hartree-Fock (HF) ab initio calculations for a series of zeolite topologies (ABW, CAN, CHA, EDI, and NAT) (84).

A correlation between the chemical shift and the Si-O-Al bond angle has been proposed based on results obtained for NaA and Na-LSX (77). Use of a similar correlation by Bull et al. for Sil-FER did not lead to the correct assignment of the resonances, and no simple correlation between the shift and any geometrical parameter (bond angles and bond lengths) could be established (14). The correlation similarly does not hold for Sil-Y and a number of other

silicates. Ab initio calculations of the chemical shifts with both HF and density functional theory (DFT) methods for Sil-FER showed that the calculations were only accurate to approximately 2 ppm (14). A major source of error was shown to arise not from the level of calculation but from the structural model used for the calculation, with small changes in bond angles between different models of only 1.2° leading to changes in the chemical shifts of as much as 3.6 ppm. Better fits between the calculated and experimental shifts of Sil-FER were obtained for ^{29}Si; the larger vibrations of the oxygen atoms were thought to be one source of the larger error for ^{17}O. Nonetheless, the accuracy of the calculated ^{17}O shifts and QCCs for the 10 crystallographic sites were sufficient to assign the spectrum partially. The authors suggested that a comparison between calculated and experimental chemical shifts (^{17}O and ^{29}Si) could lead to a method for more accurate structure determination, particularly when the approach is incorporated into a structure refinement based on diffraction data.

The shifts also vary significantly as a function of the hydration level and the nature of any nearby extraframework cations. This further complicates the assignments of the spectra but should lead to more detailed chemical information, providing that factors controlling the shifts and the QCCs are correctly unraveled. The MQMAS spectra of hydrated and dehydrated CaA (Si/Al = 1) are shown in Fig. 5. Unlike NaA, the calcium-exchanged forms of A contain "bare" oxygen atoms that are not coordinated to a cation [the O(1) sites in CaA]. These sites will be hydrogen bonded to water in the hydrated zeolite, providing one explanation for the large shift of the resonance at 45 ppm in the isotropic dimension of the MQMAS spectrum, to 75 ppm on dehydration (79). ^{17}O/^{23}Na double-resonance (TRAPDOR) NMR experiments for partially exchanged Ca(Na)A zeolites, which still contain significant numbers of residual sodium cations (i.e., with compositions such as Ca_4Na_4A), confirmed that the sodium cations are not directly bound to this oxygen site, consistent with the assignments (79). Similar behavior was found for the Sr^{2+}-exchanged form of NaA.

E. Use of Double-Resonance Experiments to Measure Connectivity and Internuclear Distances

1. Applications to Framework Structures

Many of these double-resonance experiments exploit the heteronuclear dipolar couplings between sets of spins, whose magnitudes are proportional to the inverse third power of the internuclear distance (see Sec. IV) and are therefore extremely sensitive to the distance between the coupled spins. These methods have been used (a) as a tool to assign the resonances due to different local environments and (b) to determine the connectivities between different sites in the structure. For example, spin-echo double resonance (SEDOR) has been used to determine the ^{27}Al-^{31}P distances in aluminophosphate molecular sieves (85). The high-resolution (MAS) methods termed rotational echo double resonance (REDOR) (86) and transferred echo double resonance TEDOR (87) have been applied to probe Al/Si connectivities in zeolites (88). Larger dipolar couplings were seen for silicon local environments containing larger numbers of aluminum atoms in the neighboring tetrahedral site. Connectivities between the different framework sites could then be inferred from the distance measurements extracted from these studies. INEPT experiments, which directly probe bonding between the two atoms of interest (via the J coupling), have been used to study ^{29}Si/^{27} Al connectivities (89). Fyfe and coworkers used a combination of methods (^{1}H-^{29}Si CP-INADEQUATE and ^{1}H/^{19}F/^{29}Si triple-resonance CP, REDOR, and TEDOR NMR) to study the siliceous zeolites tetrapropylammonium fluoride silicalite-1 (90) and octadecasil (91). The location of the fluoride ion was determined by measuring a series of F-Si distances between the fluoride ion and the different framework sites (90).

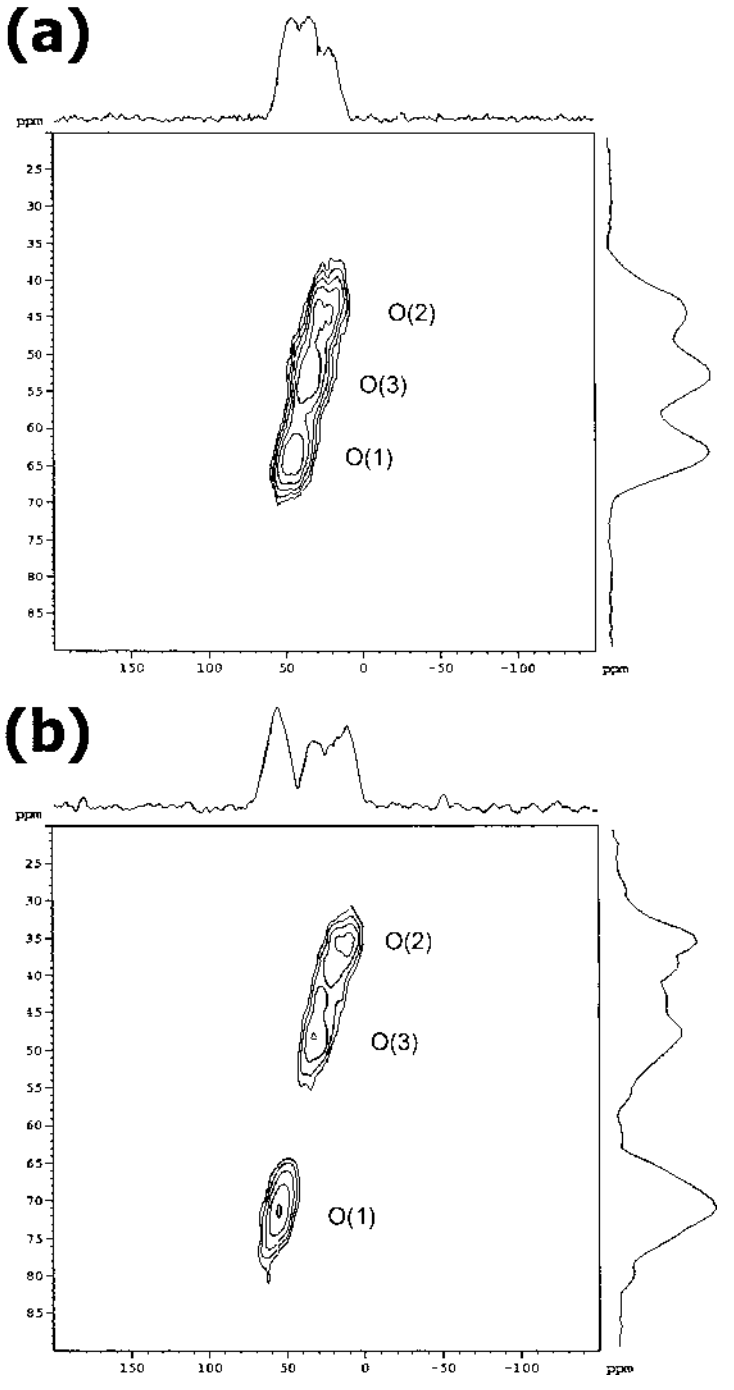

Fig. 5 Two-dimensional, triple-quantum, ^{17}O MQMAS spectra of (a) hydrated and (b) dehydrated CaA after shearing. Spectra were acquired at a field strength of 14 T, with the z-filter pulse sequence Ref. (191).

Reimer and coworkers have made use of the SEDOR experiment to measure distances between framework aluminum sites and extraframework cations. An Al-H bond length of 2.43 ($\pm$0.03) Å between the Brønsted acid proton and the nearby framework aluminum atom was measured with a ^{1}H-^{27}Al SEDOR experiment (92). ^{27}Al-^{35}Cu SEDOR NMR has been used to show that the Cu^{+} cations in copper-exchanged ZSM-5 are located only 2.3 ($\pm$0.2) Å from the aluminum framework sites (93) and are thus associated with these sites. ^{27}Al-^{207}Pb SEDOR NMR has also been used to study a series of lead-exchanged zeolites and the measured Pb-Al distances were consistent with XRD studies (94). The ^{207}Pb spectra were strongly affected by hydration level, and the presence of both $PbOH^{+}$ and Pb^{2+} cations (in equilibrium) was proposed. The $PbOH^{+}$ species is similar to that found in CaY that has not been completely dehydrated (95). Rotational echo and adiabatic passage double resonance (REAPDOR) (96) has been used to measure ^{29}Si/^{23}Na distances between framework atoms and extraframework Na^{+} cations in titanosilicates (97).

2. Applications to Gas Binding and Cluster Formation in the Zeolite Pores

These methods can be used, in principle, to determine how a molecule coordinates to the framework of the zeolite by measuring a series of key internuclear distances. For example, Lobo and coworkers have used ^{1}H/^{27}Al and ^{1}H/^{29}Si REDOR and ^{1}H/^{29}Si CP experiments to investigate Al-ZSM-12 synthesized by using the selectively labeled deuterated benzyltrimethylammonium cation as the SDA (32). A series of REDOR decay curves were obtained for samples loaded with either SDA cations containing deuterated methyl groups or benzyl groups or the fully deuterated SDA. The methylene protons were found to be preferentially located near $Si(OSi)_3(OAl)$ silicon atoms, suggesting that the aluminum atoms themselves must be directly associated with the SDAs. Ba et al. have used ^{29}Si-^{27}Al REAPDOR methods to investigate the formation of silicon nanoclusters inside the pores of zeolite Y (98).

Even if accurate internuclear distances may not be readily obtained [due to residual motion of the molecules, or multiple spin systems (99)], measurement of the relative distances (or dipolar couplings) between sets of spins is often sufficient to distinguish among different structural models. ^{19}F/^{23}Na CP MAS NMR experiments have been used to study the binding of the hydrofluorocarbon CF_3CFH_2 (HFC-134a) and CF_3CF_2H (HFC-125) and CF_2HCFH_2 (HFC-143) to zeolite NaY. Individual CP buildup curves for the two end groups of the asymmetrical molecules could been determined by exploiting the very large differences in ^{19}F chemical shifts for the two ends of the molecules (Fig. 6). These double-resonance experiments showed very different binding for the different end groups and demonstrated that the hydrogen-containing groups are bound more strongly to the zeolite framework in the order $CF_3 << CF_2H < CFH_2$ (100,101).

F. NMR Studies of Extraframework Cations

The extraframework cations in zeolites can play an important role in determining the adsorption, separation, and catalytic properties of zeolites. The distribution of the cations controls the electric fields inside the pores of the zeolites, which can strongly influence absorptive behavior and catalytic activity. Thus, characterization of the location and occupancies of the cation sites is a prerequisite for understanding the physical properties of zeolites. NMR can play an important complementary role to diffraction in this area, particularly for zeolites with more than one type of cation (e.g., Na^{+} and Cs^{+}), where it can sometimes be difficult to distinguish between the different cations. NMR can be used to follow the cation-exchange procedure and identify cations that are not removed during the ion-exchange reaction(s).

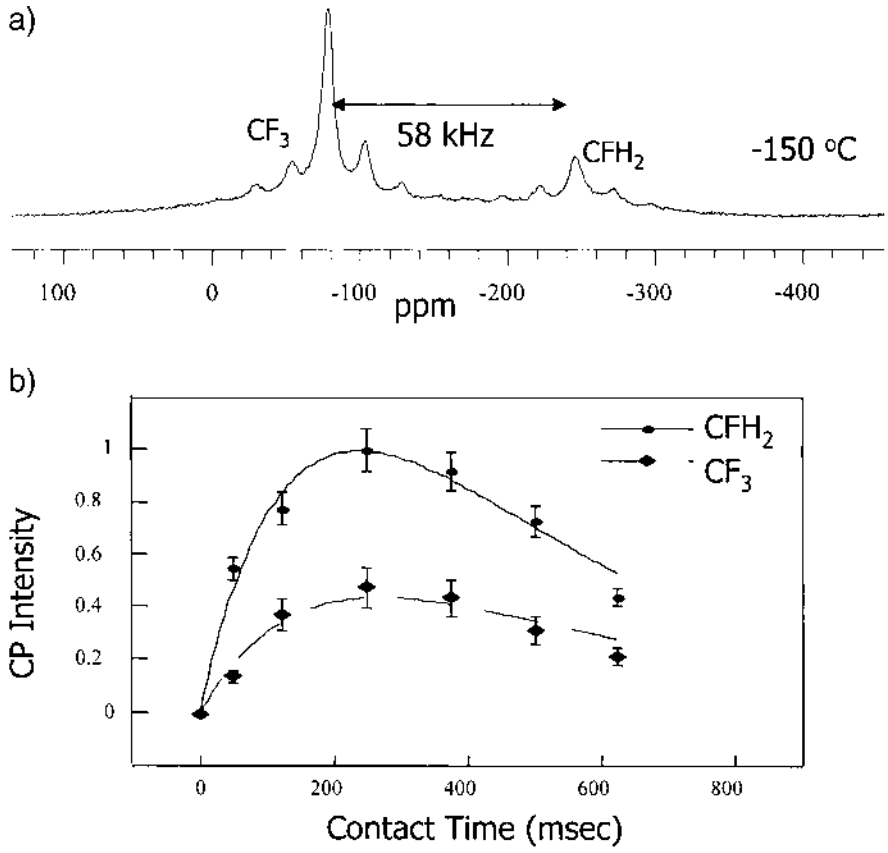

Fig. 6 (a) The ^{19}F MAS NMR spectrum of CF_3CFH_2 (HFC-134a) sorbed in dehydrated zeolite NaY at −150°C. (b) A plot of the $^{19}F/^{23}Na$ CP intensity of HFC-134a in NaY as a function of the contact time, for ^{19}F irradiation at the CF_3 and CFH_2 frequencies. Both the one-pulse and CP spectra were acquired at −150°C (100,101).

1. Sodium

The sodium forms of zeolites have been widely investigated by NMR, in part due to the sensitivity of the $I = 3/2$ ^{23}Na nucleus to the sodium local environment. However, the interpretation of the one-pulse ^{23}Na MAS NMR spectra is not straightforward primarily due to the broadening caused by the second-order quadrupolar interaction, which leads to considerable overlap of the resonances. DOR has been widely employed to obtain high-resolution ^{23}Na NMR spectra (102–106). More recently, MQMAS techniques have also been used to investigate the locations of the sodium cations in NaY (Si/Al: 2.4 and 2.6), NaEMT (3.7), NaMOR (7.1), and NaZSM-5 (18.0) (107,108). The ^{23}Na NMR parameters can be determined more accurately when both MQMAS and single-pulse MAS NMR are used by comparing the quadrupole parameters obtained from the shifts of the NMR resonances in the isotropic dimension of the two-dimensional MQMAS NMR spectrum with those obtained from the one-dimensional MAS spectrum (109). The inherent problems in quantifying the MQMAS spectra can be overcome by simulating the ^{23}Na one-pulse spectra (Fig. 7) with the NMR parameters obtained from the MQMAS data (Fig. 8; see below). This is discussed in more

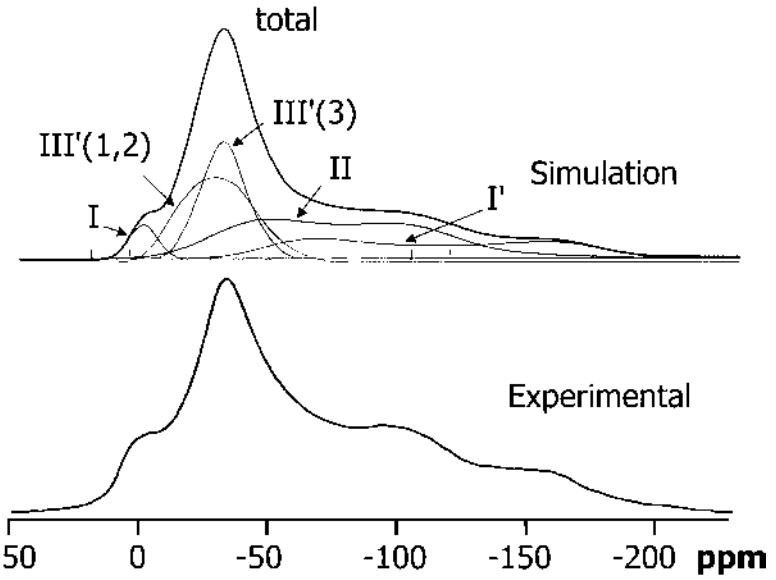

Fig. 7 The isotropic resonances seen in the ^{23}Na MAS NMR spectrum of dehydrated NaX acquired at a spinning speed of 21 kHz. Simulations of the isotropic resonances were performed by using values for the quadrupolar parameters and isotropic shifts for the different cation sites obtained from the MQMAS spectrum (shown in Fig. 8; see Sec. IV for more details).

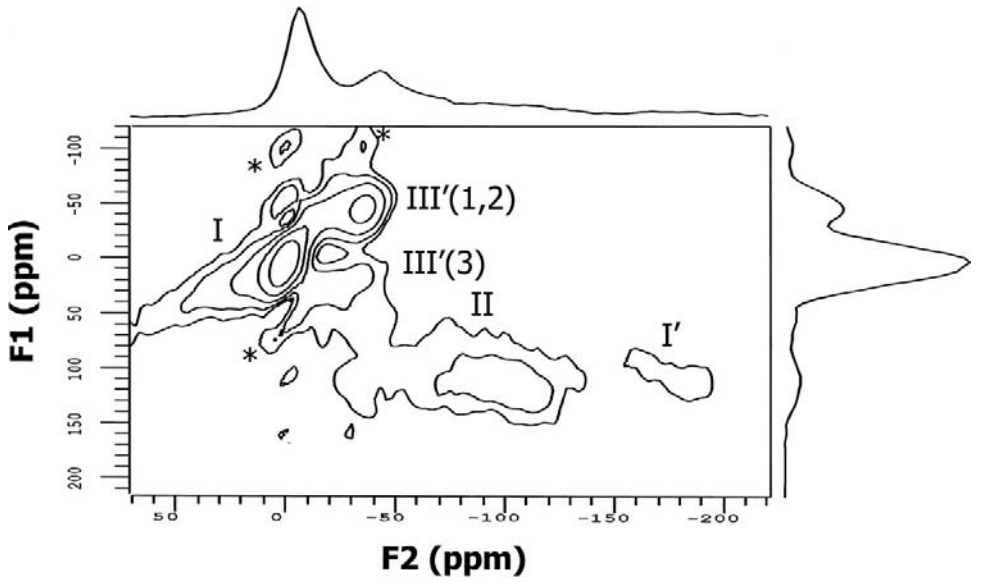

Fig. 8 2D ^{23}Na triple-quantum MAS NMR spectrum of dehydrated NaX, after shearing. Projections on the isotropic (F1) and anisotropic (F2) dimensions are shown. The asterisks mark the artifacts originating from the collection of insufficient data points. A ^{23}Na radio frequency field strength of 200 kHz and a spinning speed of 21 kHz were used.

detail in Sec. IV. However, the intensities extracted from the isotropic resonances may still require correction to compensate for any intensity of the central resonance that is contained in the spinning sidebands. The approach of Massiot et al. has been widely used for this, but possibly the easiest approach is to simulate the spectra with one of the many available NMR simulation programs. The corrections can be negligible for very fast spinning speeds particularly at higher fields (110).

Most studies have focused on the faujasite zeolites NaX and NaY. The typical cation positions in faujasite zeolites such as NaX and Y have been determined by X-ray diffraction (XRD) and neutron diffraction (Fig. 9) (111–114). Sites I and I′ are located in the hexagonal prism and the sodalite cage, respectively, while the site II and III positions are in the supercage. In dehydrated zeolite NaY, the sodium cations are mainly located on the site I, I′, and II positions (111,112). Sodium cations are also found in several sites close to the site III position, in dehydrated NaX. A QCC of 1.2 MHz was found for the SI cations in NaY and NaEMT, from MQMAS experiments, which was much larger than expected for a cation located in the highly symmetrical environment at the center of the hexagonal prism, as proposed based on XRD experiments. These results suggest that the site I position is displaced from the center of the hexagonal prism, resulting in the large QCC value (115). This has been observed by XRD for Zn^{2+} substitution in the SI position (47).

Two types of I′ sites, with slightly different local environments, were observed in an XRD study of a single crystal of NaX (Si/Al: 1.18) (113). This can be rationalized as follows: A six-membered ring in the faujasite structure is made up of, at most, three aluminum atoms per ring. If the six-membered rings that contain zero or only one aluminum atom (which represent the least probable arrangements in NaX zeolites) are ignored, then approximately 24 and 8 six-membered rings per unit cell have three and two aluminum atoms per ring, respectively, for an Si/Al ratio of 1.18 ($Na_{88}Si_{104}Al_{88}O_{384}$). Site I′ sodium cations can be coordinated to both of

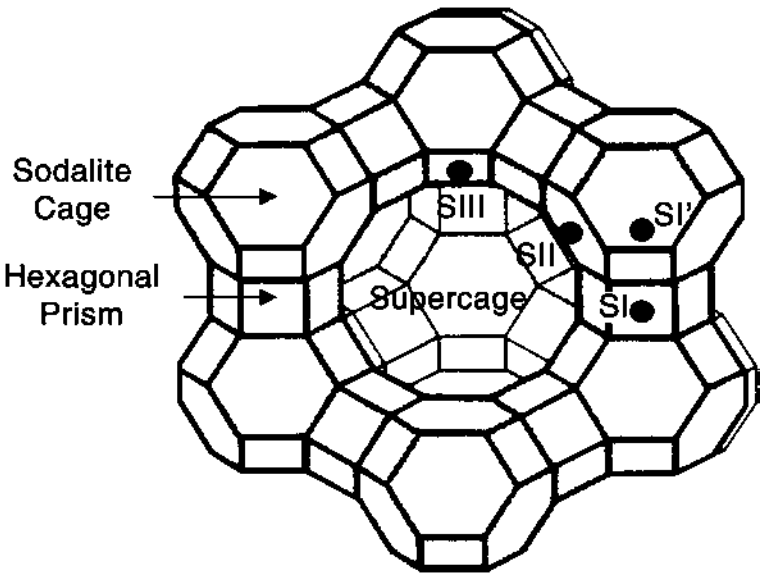

Fig. 9 The faujasite structure (adopted by zeolites Y and X), showing some of the typical cation positions.

these types of six-membered rings (113). Electric field gradient (EFG) calculations have shown that the QCC for the site I′ sodium cations coordinated to the six-membered rings containing three aluminum atoms (5.0 MHz) is larger than that for the site I′ cations coordinated to the rings with only two aluminum atoms (3.6 MHz) (102). The ^{23}Na DOR NMR spectrum of NaX (Si/Al: 1.23) could be well reproduced by a computer simulation that used ^{23}Na NMR parameters for six different sodium cations [site I, II, and III′ (two sites), and the two types of site I′ cations] (102). However, the DOR spectra are not always unambiguous due to overlap between the isotropic resonances and the sidebands, which is difficult to avoid due to the limitations in the maximal spinning speed of the outer DOR rotor (approximately 1 kHz). The sodium cations at the site I′ in zeolite NaY are not easy to detect by MQMAS NMR spectroscopy due to their large QCCs. Nonetheless, experiments using higher radio frequency (rf) field strengths (109) or by using the O-RIACT MQMAS pulse sequence (110) have succeeded in observing these resonances. For example, Fig. 8 shows the MQMAS spectrum of NaX. Two different SIII positions are seen, along with a weaker resonance for the SI' cations. A resonance due to the second I′ environment was not detected in these studies. All of these studies show distributions in QCCs and chemical shifts for the different sodium local environments; this results in characteristic MQMAS lineshapes, in which the broadening due to a distribution of QCCs and a distribution of shifts can be readily distinguished. The environments are clearly sensitive to aluminum distributions in the framework and the nature of the nearby cations. For example, the QCC of the major SII environment increases from 3.9 ($\pm$0.15) MHz in NaY to 4.9 ($\pm$0.15) MHz in NaX (109). Care is clearly required in interpreting these spectra, as it cannot always be assumed that each cation site identified by crystallography will necessarily correspond to a single ^{23}Na resonance.

Having identified the NMR parameters for the different cation positions, the method can be used to investigate gas binding. For example, ^{23}Na MQMAS spectroscopy was used to follow the effect of sorption of HFC 134 (CF_2HCH_2H) on the sodium cation positions (109). The resonance due to the SI' cations was no longer observed in the MQMAS spectrum, which was somewhat surprising, given that these cations are not initially accessible for gas binding. The results were, however, consistent with earlier diffraction and ^{23}Na MAS NMR experiments on the same system, which indicated long-range cation migration out of the sodalite cages and into the supercages occurs, with the extra sodium cations occupying SIII-type sites (116). Variable-temperature experiments indicate that the cation positions are not held rigidly to the framework, with exchange between all the sites occurring at temperatures as low as 250°C (109).

2. Cesium and Lithium

The cesium- and lithium-exchanged Y and X zeolites have also been extensively studied by NMR. The 100% abundant ^{133}Cs (I = 7/2) nucleus is very sensitive to its local environment, as demonstrated by its large chemical shift range (117). The quadrupole coupling constants at ^{133}Cs sites are typically very small, and hence the broadening of the ^{133}Cs resonances, due to the second-order quadrupolar interaction, is very small. ^{133}Cs is therefore a favorable nucleus to use for study of the short-range ordering of extraframework cation sites in zeolites. Several studies of dehydrated CsNa-Y zeolites have found cesium cations in various sites of the faujasite framework (118–120). Some discrepancy in the assignments of the different ^{133}Cs resonances to the different cation sites exists in the literature. This appears to be related to (a) the sensitivity of the ^{133}Cs chemical shift to small changes in the local environment (e.g., differences in the numbers and arrangements of the framework aluminum atoms near to cations, or differences in the numbers and types of nearby extraframework cations), (b) residual water in the nominally dehydrated material, and (c) mobility of the cesium ions in the cages (119,120).

In the lithium (121–125), sodium (126), and cesium systems (127), the assignment of the resonances has been aided by investigating samples loaded with the paramagnetic molecule, O_2, either by cooling the sample in air or by loading controlled levels of the gas. The interaction between the cations and oxygen molecules leads to shifts in the cation NMR resonances. Since only cations in the supercages of faujasite zeolites can bind the oxygen molecules, supercage vs. sodalite cage resonances can be readily distinguished (Fig. 10) (127). For example, the room temperature spectrum of Cs-exchanged NaY acquired in air shows three resolved isotropic resonances at −74, −90, and −155 ppm. These are assigned to two different types of SII Cs^+ cations in the supercages (with the two peaks likely arising from differences in the number of neighboring Al atoms in the cation local coordination environment) and SI' Cs^+ in the sodalite cages (119), respectively. As the temperature is lowered, the resonances due to cesium in the supercages shift dramatically to lower frequencies, primarily due to increased O_2 loading and increased magnetic susceptibility of the O_2 molecules. The SIII resonance is clearly resolved at −40°C and below, and both the SII' and SI' sites become clearly visible at −150°C at −122 and −148 ppm, respectively (127). O_2 sorption studies of lithium-exchanged FAU zeolites have shown that only the SIII/SIII' cations interact with the oxygen atoms. The SII cations are tucked into the 6-ring of the supercage and, in contrast to the cesium and sodium cations, are no longer accessible (122,125). These studies have also shown that the Li^+ cations in the SIII/SIII' sites are highly mobile (123).

^{133}Cs NMR, in conjunction with in situ XRD, has been used to follow the Cs^+ ion-exchange of NaY (119). Cesium cations (ionic radius = 1.7 Å) are only able to exchange with the sodium cations in sites located in the supercages of X and Y zeolites, since the entrance to the

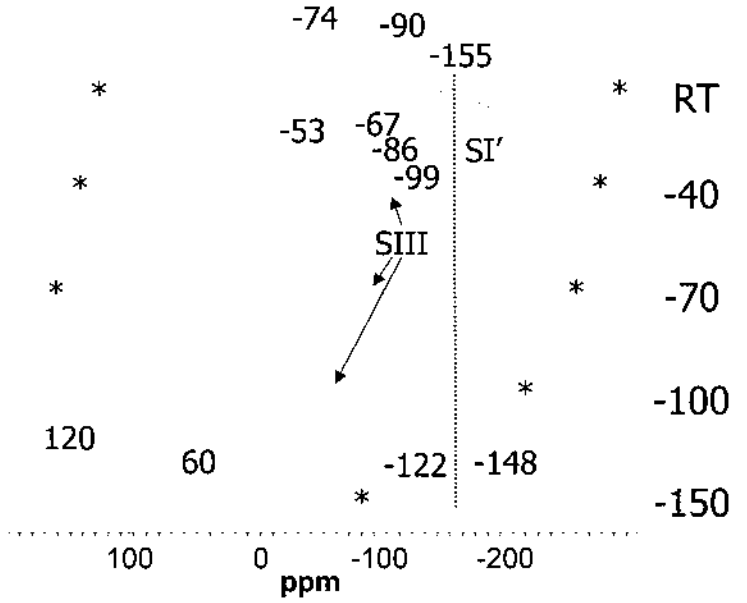

Fig. 10 ^{113}Cs MAS NMR spectra of dehydrated Cs-Y spun acquired in air at various temperatures. The asterisks denote spinning sidebands. The sample of CsY was prepared from NaY by three ion-exchange + dehydration steps. Following each ion-exchange reaction (with 0.1 M $CsNO_3$), the sample was calcined at 450°C.

sodalite cage (2.2 Å) limits the passage of cesium cations into the sodalite cage during the ion-exchange process. Not until the sample is heated to 350°C and above do the cations migrate from the sodalite to the supercages. This is accompanied by an increased intensity of the resonances at −130 to −150 ppm due to the SI' and SII Cs cations (Fig. 11). This is followed by the migration of the residual sodium cations in the sodalite cages into the supercages (SII) and SI positions. This latter process can be monitored with ^{23}Na NMR. The differences in chemical shifts due to environments assigned to SII and SIII cations in Fig. 10 and 11 result from small changes in the Cs/Na cation ratio and the distributions of the Cs and Na cations in the different cages.

3. Rubidium

The quadrupole moment of the $I = 3/2$ ^{87}Rb is larger than that of ^{23}Na making identification of the different ^{87}Rb resonances difficult. However, the method has been used to follow the progress of solid-state ion-exchange reactions in faujasite zeolites (128).

G. ^{1}H MAS NMR Studies of Zeolites

^{1}H MAS NMR has been widely exploited to investigate acidity, and the defects in the zeolite framework, created during synthesis, dehydration, or the catalytic reaction. ^{1}H MAS NMR has

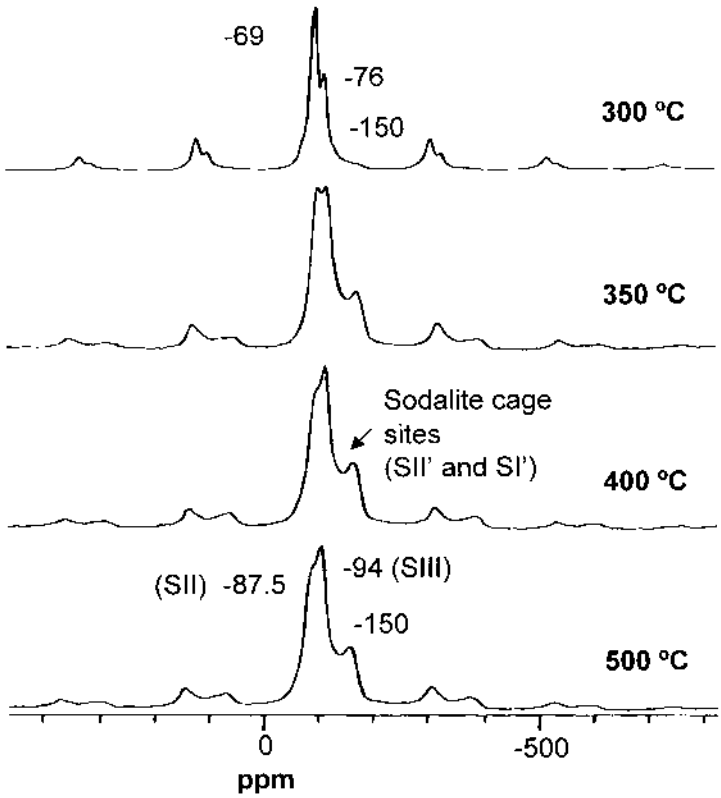

Fig. 11 Room temperature ^{133}Cs MAS NMR spectra of cesium exchanged NaY, after the first ion-exchange reaction and subsequent dehydration at 300, 350, 400, and 500°C. All of the isotropic resonances lie in a chemical shift range from −60 to −150 ppm. All the other peaks are spinning sidebands, which primarily arise from the satellite transitions.

also been used to follow the progress of the catalytic reaction. Acidic zeolites (HZ) are typically created by dehydration of the ammonium-exchanged form of the zeolite:

$$(NH_4)Z \rightarrow HZ + NH_3(g)$$

Typical ^1H chemical shifts for environments found in zeolites are listed in Table 2. Notable exceptions to these general trends exist. For example, a resonance has been observed at 7.5 ppm, along a more intense resonance at 4.5 ppm, in some samples of H-ZSM-5 (129), which have both been assigned to Brønsted acid protons. Although the chemical shifts of protons in silanol and aluminum oxide (Al-OH) extraframework species overlap, $^1H/^{27}Al$ TRAPDOR NMR may be used to determine whether the proton is near a ^{27}Al spin and thus separate these two species (56,95).

Acquiring ^1H MAS NMR of zeolites requires careful preparation of the sample. The spectra of hydrated zeolites will be complicated by the rapid exchange that often occurs between water and many of the proton-containing species. For example, zeolites containing Brønsted acid sites, NH_4^+ ions, and water, will show only one resonance with a chemical shift that represents the average chemical shift position for the three species, weighted by the appropriate concentrations of the three species (128). At the other extreme, prolonged dehydration of many aluminum-rich zeolites at high temperatures can result in significant dealumination and a loss in the number of Brønsted acid sites (130).

Samples that have only been partially dehydrated can often show narrow resonances at approximately 4.6–4.8 ppm due to water (95). These resonances can be distinguished from those due to Brønsted acid sites because they show little or no $^1H/^{27}Al$ TRAPDOR effect. In addition, very characteristic sideband patterns may be observed at low temperatures where the water motion is frozen out. Sideband patterns resembling a Pake doublet have been observed, the splitting [i.e., the width of the resonance] being caused by the dipolar coupling between the two ^1H spins of water (95).

Haw *et al.* have shown that the shifts may be strongly affected by hydrogen bonding to sorbed species (131). For example, strong hydrogen bonding to a sorbed molecule such as acetylene results in a dramatic shift of the Brønsted acid proton from approximately 3.8 ppm to 7.3 ppm (131). The shift is highly dependent on the concentration of the sorbed base and on temperature. At ambient temperatures, the shift arises from the rapid exchange between the bound and free base, with the shift increasing as a function of loading level until a saturation value is achieved; at lower temperatures two resonances can be resolved, one due to the free base and the other from the hydrogen-bonded complex. Haw and Nicholas have performed DFT ab initio calculations on a series of molecules and ions sorbed on representative zeolite frameworks to determine the structures and calculate the ^{13}C chemical shifts of the sorbed

Table 2 Typical Ranges for the ^1H Chemical Shifts (ppm) of Some Different Species Found Zeolites

Species	Chemical Shift
(NH_4^+) and protonated amines	6.0–8.1
Non-hydrogen-bonded silanols	1.2–2.3
Hydrogen-bonded silanols	2.5–12
Brønsted acid sites	3.0–5.0
Al-OH nonframework species	1.2–3.6
Water	4.6–5.0

Source: Refs. 2,56,95,130, and 234–236.

molecule–zeolite complexes (132,133). Figure 12 shows the extremely large shift in the ^{1}H chemical shift of the Brønsted acid site (originally at 4.3 ppm) that occurs on sorbing nitromethane and deuterated acetone in H-ZSM-5. The larger shift for the Brønsted acid site that is hydrogen bonded to acetone (18.6 ppm) in the presence of sorbed nitromethane suggests that the interaction between the two sorbents leads to an additional degree of proton transfer from the zeolite to the sorbent. These ^{1}H NMR results were consistent with changes in the ^{13}C chemical shift of acetone in the presence and absence of nitromethane. DFT calculations were again used to explore the effects of the coadsorbates on zeolite acidity. For example, Fig. 12d shows the gas phase structure of the nitromethane acetone complex, following protonation of the acetone. Protonation of this complex was calculated to be 16 kcal mol^{-1} more favorable than protonation of acetone alone. Addition of nitromethane into a catalytic flow reactor resulted in enhanced activities for a series of acid-catalyzed reactions (e.g., methanol and isopropanol conversions), consistent with the increase in apparent zeolite acidity.

An even stronger interaction with the Brønsted acid proton (i.e., sorption of a stronger base) results in the transfer of the proton from the zeolite framework to the sorbed base:

$$B\text{---}HZ \rightarrow BH^{+}\text{---}Z^{-}$$

A *decrease* in the chemical shift is then seen, with the shift of the proton now depending on the base and its interaction with the Brønsted acid site. For example, the ^{1}H shifts of protonated monomethylamine range from 6.8 to 8.0 ppm, with the shifts presumably depending on the strength of hydrogen bonding of the proton, now on the protonated base molecule, to the

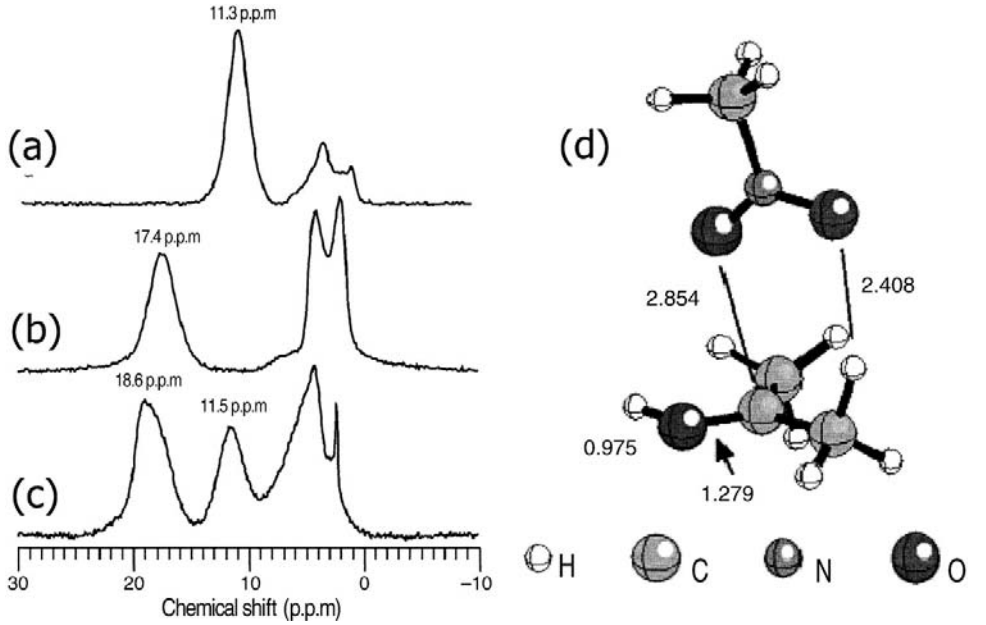

Fig. 12 The ^{1}H MAS NMR spectrum of HZSM-5 loaded with (a) nitromethane, (b) acetone-d_6, and (c) acetone-d_6 and nitromethane, showing the effect of hydrogen bonding on the ^{1}H chemical shift of the Brønsted acid site (originally at 4.3 ppm). The spectra were acquired at 77 K at a spinning speed of 10 kHz. (d) A DFT calculation of the protonated acetone-nitromethane complex formed in the gas phase, illustrating some of the interactions that result in enhanced proton transfer from the zeolite to the sorbed acetone molecules. (Reproduced from Ref. 133).

zeolite framework (57). The shift of the probe molecule resonance to higher frequencies, with increased strength of hydrogen bonding, and the subsequent decrease as the proton is transferred has resulted in some difficulty in determining whether a shift is indicative of proton transfer or strong hydrogen bonding, particularly for sorption of weaker bases such as water and methanol. All of these results are highly dependent on the temperature and the loading level (see below). At higher loading levels, where the numbers of sorbed bases exceeds the number of acidic sites, an average chemical shift is observed (56,134). Again, ab initio (DFT and HF) methods have been used to help rationalize the NMR observations (135).

H. Probe Molecule Studies of Acidity and Basicity

An understanding of acid strength, and the role of the framework in controlling this, is fundamental to the understanding of acid-catalyzed reactions in zeolites. The nature and numbers of acidic sites can be studied by investigating the interactions of basic molecules sorbed on zeolites by ^{13}C, ^{15}N, and ^{31}P NMR spectroscopy (136–139). The ^{15}N and ^{31}P chemical shifts of a series of bases such as trimethylphosphine (TMP) (137,140) monomethylamine (MMA) (57), and pyridine (141) are significantly different depending on whether the base is coordinated to a Lewis acid site, physisorbed, or whether the base is protonated by the Brønsted acid proton, allowing the concentrations of different types of sites to be determined. Research in this area has been reviewed (142,143). Experiments involving sorption of phosphines and phosphine oxides on zeolites (57,140,144) are easier to carry out than those involving amines in view of the sensitivity (large γ and 100% natural abundance) of the ^{31}P nucleus. No isotopic labeling is required. Furthermore, binding of molecules such as TMP is less complicated than binding of some other widely studied basic molecules such as water, methanol, and many amines because extensive hydrogen-bonding networks are not formed.

All of the NMR results are highly dependent on the temperature and the loading level (56,134,145,146). At low loading levels (i.e., where the loading level is lower than the available number of Brønsted acid sites) of a strong base such as an amine or a phosphine, where hydrogen transfer occurs, the protonated base remains bound to specific sites of the framework (at least at ambient temperatures). At higher loading levels, the mobility of the bases increases dramatically, hydrogen bonding between the nonprotonated bases and the protons in the protonated bases allowing for rapid transfer of protons between molecules and for increased mobility of the molecules and ions. This motion can be frozen out at lower temperatures, and resonances from the individual components can be resolved. Phosphine oxides tend to be less mobile than phosphines and rigid complexes are often observed, even at room temperature (144,147).

More recently, a series of double-resonance experiments have been performed that allow the connectivities or distances between spins on the site of adsorption and on the adsorbed molecule to be determined (148–151). ^{15}N-^{27}Al REDOR NMR has been used to measure the distance between the aluminum T sites in zeolite HY and the nitrogen atom in ^{15}N-enriched MMA (150). The measured ^{15}N-^{27}Al distance of 3.1 Å was consistent with models for $MMAH^+$ binding involving two or three hydrogen bonds as predicted by the calculations of Teunissen and van Santen for NH_3 binding on acidic zeolitic clusters (152,153). The sorption of a probe molecule such as MMA reduces the QCC of the aluminum site, and hence the second-order quadrupolar interaction, significantly (53,56). This means that aluminum spins are now clearly visible, even at moderate fields, in a standard MAS experiment, and experiments may be performed where these spins are observed directly. One aluminum atom becomes ''visible'' per adsorbed probe molecule (56). Thus, in these types of systems, the fraction of visible aluminum should be accurately determined in order to analyze the REDOR data. Solid-state NMR methods and ab initio calculations have been employed to investigate the structure of the

trimethylphosphine (TMP)–Brønsted acid site complex in zeolite HY (151). $^{27}Al/^{31}P$ and $^{27}Al/^{1}H$ REDOR experiments performed at −150°C were utilized to measure Al-P and Al-H_B distances for the acid site–TMP complex of 3.95 (0.05) Å and 2.8–3.1 Å, respectively, where H_B is the Brønsted acid site proton (151). A more accurate measurement of the Al-H_B distance was not possible because models that assume the presence of isolated Al-H spin pairs were not valid in this case. A P-H_B distance of 1.40 (0.02) Å was obtained by fitting the spinning sidebands in the ^{1}H MAS NMR spectrum. These internuclear distances are within the range of the Al-P, Al-H, and P-H distances obtained from ab initio calculations for the ion pair (IP) $TMPH^+$–zeolite complex that is formed by transferring a Brønsted acid proton to TMP.

The Lewis acid sites in dehydroxylated HY can be observed indirectly and *quantified* by sorbing a basic probe molecule. For example, $^{15}N/^{27}Al$ TRAPDOR NMR has been used to demonstrate that the nitrogen atom in the MMA molecule binds directly to an aluminum atom in the Lewis acid site formed on hydroxylation (or steaming), and to determine a QCC of 8.5 MHz for this Lewis acid–MMA complex (56). $^{27}Al/^{31}P$ TRAPDOR methods have also been used to study the binding of the probe molecules trimethylphosphine oxide (144) and TMP (57) to the Lewis sites in dehydroxylated HY and USY. For example, Fig. 13 shows the $^{31}P/^{27}Al$ TRAPDOR NMR of trimethylphosphine sorbed on HY dehydrated at 600°C. The ^{31}P resonance due to TMP bound to the aluminum Lewis acid site (at −46 ppm) is clearly resolved in the "difference" spectrum. The resonances for TMP sorption on the Brønsted and

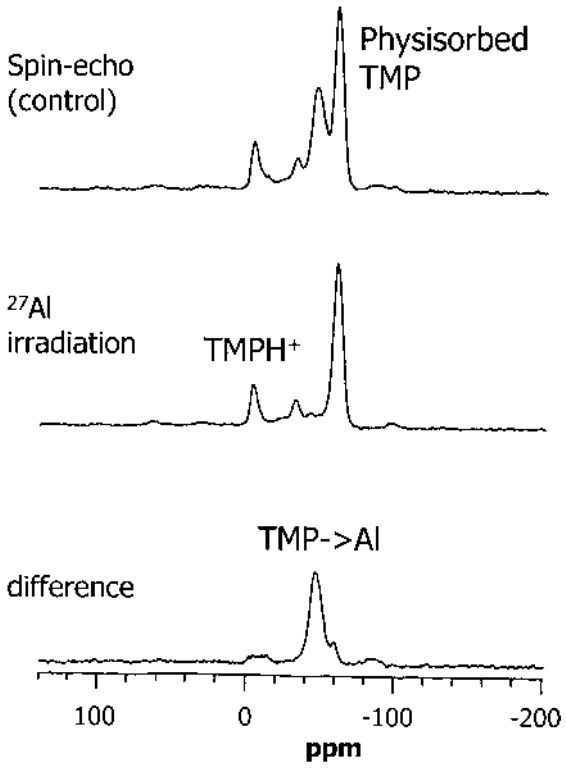

Fig. 13 The $^{31}P/^{27}Al$ TRAPDOR spectra of trimethylphosphine sorbed in HY obtained (top) without and (middle) with ^{27}Al irradiation at −150°C. The difference spectrum, i.e., top minus middle, is shown in bottom. ^{27}Al irradiation was applied for 725 μs and a spinning speed of 5520 Hz was used.

Lewis acid sites may be resolved and the concentrations of these two sites may be readily determined as a function of the sample preparation method. INEPT experiments have been used to observe a ^{31}P-^{27}Al J-coupling between the aluminum Lewis acid surface site and the bound molecule (TMP) (154). A ^{31}P-^{27}Al J-coupling constant of 270 ($\pm$10) Hz was determined, which is consistent with a five-coordinated aluminum Lewis acid–TMP complex, and thus a four-coordinated Lewis acid site. The INEPT experiment represents an alternative approach for probing the strength of these acid–base complexes, since the J coupling is a measure of the interaction between the phosphorus and aluminum atoms.

The mobility of the probe molecules has been studied by many authors. For example, in the TMP-zeolite system, Lunsford et al. showed that the motion of $TMPH^+$ complexes in zeolites such as HY, dealuminated HY, and HZSM-5 was strongly affected by the size of the cavities and/or channels, and the temperature of the sample (155). The motion of TMP has also been studied as a function of temperature by Bendada et al. (156) and by Kao et al. (57,95). Exchange between different binding sites could be frozen out at low temperatures (57,95). This mobility has important implications for the double-resonance experiments (90,150,157).

NMR methods for measuring internuclear distances are based on a determination of the dipolar coupling between two spins. In the absence on any motion, this dipolar coupling is inversely proportional to the cube of the distance between the spins. However, the dipolar coupling, even between nearby spins, is often very small on the time scale of many motional processes, *e.g.*, a ^{27}Al–^{15}N distance of 3.1 Å corresponds to a dipolar coupling of only 0.1 kHz (150). Thus, any residual motion at or faster than this time scale (generally more than 1–10 ms) will reduce or, for isotropic motion, average the measured dipolar coupling constant to zero, resulting in a longer than expected distance. This typically requires that any experiments involving molecules sorbed on surfaces be performed at low temperatures, where the translational motion of the molecules will be frozen out. Any remaining motion (*e.g.*, librations) of the molecule on the surface will similarly reduce the measured internuclear distance, and in some circumstances it may be appropriate to consider the NMR experiment as a method for determining the maximal internuclear distance between spins. Fyfe and Lewis have also discussed the need to consider mobility of the probe molecules when measuring internuclear distances between sorbent and substrate (90,157).

NMR has also been used to probe basic sites in zeolites. Probe molecules such as pyrole and chloroform have been used to probe interactions with the framework oxygen sites (158,159). For chloroform and other chlorocarbons such as CF_2HCF_2Cl, the shift in the ^1H resonance provides clear evidence for hydrogen bonding to the basic zeolite framework sites (160,161). ^{13}C NMR has been used to study the methoxy groups formed on reaction of a halocarbon or methanol with the zeolite framework, providing an alternative method for investigating the basicity of different framework sites or zeolites (162–167). The basic zeolites contain extraframework cations, which can dramatically alter the basicity of the framework oxygen sites and play an important role in the catalytic reaction. The interactions of the probe molecules with these cations need to be considered when interpreting the NMR results; however, NMR can play an important role in sorting out the strength or importance of the different interactions (168).

III. PRACTICAL CONSIDERATIONS

A. Controlling the Sample Environment

Many studies of zeolites require that the materials be studied under controlled atmosphere (to prevent moisture entering the sample, or to prevent sorbed gases from escaping). This presents a

challenge if MAS experiments are to be performed. Klinowski et al. and others have studied catalytic reactions of, e.g., methanol in H-ZSM-5 (169) by sealing the samples in glass ampules, which are designed so that they fit snugly into the NMR rotors (170). This technology is most easily implemented in the Chemagnetics design of pencil probes, where sleeves can be readily fabricated to hold the ampoules in place. Glass ampules are typically sealed by cooling the sample with liquid nitrogen and then flame sealing, or by using glue to seal a constricted tube; both methods lead to possible errors in quantifying the gas loading level. Glass ampules sealed under vacuum can also suffer from heat conduction problems, resulting in differences between the measured and actual temperatures that are much larger than those typically observed for a fully packed rotor, particularly at low temperatures.

Sometimes a tight rotor cap can prove to be sufficiently airtight. At low temperatures in particular, the differential contraction of the cap and rotor can lead to leaks, and this approach may not be feasible. For example, when the low-temperature experiment is performed with air as the spinning gas, oxygen can be sorbed into the zeolite pores, leading to dramatic changes in the NMR spectra (171). Furthermore, samples packed into rotors at ambient temperatures in a glove box may pick up gases present in the glove box, and lose some or all of the previously sorbed gas. Haw et al. have solved these problems in their CAVERN design for loading rotors (132). Here the zeolite sample is first evacuated and activated in the middle section of a specially designed glass vessel. The sample is then cooled cryogenically, by placing the vessel in liquid nitrogen, and controlled loading levels of gases are introduced. A plunger can then be pulled, allowing the loaded sample to drop into the MAS rotor in the lower section of the vessel. The rotor is then capped, again using the plunger. Since the capping is performed at low temperatures, a very tight seal at higher temperatures is assured. The method also allows very accurate control of gas loading levels.

B. High-Temperature Studies of Catalysis and Catalyst Structure

High-temperature MAS experiments are severely restricted by the highest temperature reached by most commercial routine probes (250°C). Nonstandard high-temperature MAS approaches used to date include laser-heated probes (172,173) and specially designed high-temperature probes (174). The laser probes suffer from large temperature gradients and from difficulties in determining the exact temperature. Nonetheless, they have been used to study catalytic reactions in zeolites and proton mobility (175,176). They can be used for "temperature jump" experiments, which allow species that are highly reactive at high temperatures to be trapped and studied by NMR at lower temperatures (173). The DOTY water-cooled high-temperature probe uses boron nitride components and rotor caps that are screwed to the main rotor so as to overcome problems of differential expansion. For example, this probe has been used to study cation mobility up to 500°C (120). An alternative approach, developed by Sarv et al., involves spinning a long glass ampule (174). Spinning and heating are separated: one end of the ampule is held tightly by a large and heavy MAS rotor, which spins in the MAS stator. The other end of the ampule (containing the sample) sits in the coil and can be heated to a desired temperature. This probe has been used to investigate the mobility of Brønsted acid site protons.

None of these approaches is simple, and alternative setups for studying catalytic reactions have been developed where the temperature of the sample containing the sorbed gas can be rapidly quenched (in less than 200 ms) at different stages during the catalytic reaction. The sample can then be transferred to an NMR rotor in a glove box, allowing the progress of the reaction to be followed (177). The method also allows reactivity to monitored under flow conditions. This approach should be contrasted to reactivity studies performed in glass

ampules. These studies will typically monitor the formation of the thermodynamic products. For example, in the methanol-to-gasoline (MTG) chemistry that occurs over acidic zeolites, unsaturated alkenes are not typically observed, although they are seen under flow conditions; the alkenes react rapidly in these static reaction vessels (i.e., the ampules) to form the more thermodynamically favorable saturated alkanes (169). Finally, Hunger et al. have developed a MAS setup for catalysis, where the reactant gas is injected directly into a *spinning* rotor, which contains the catalyst. The rotor is open at one end, allowing for continuous gas injection throughout the experiment. The airflow is designed so that the reactant gas flows over the catalyst and out of the rotor, where it is can be detected downstream by gas chromatography (178). The method has been used to study catalytic reactions and the change in catalyst structure as a function of the reaction conditions (179,180) and can also be combined with stopped-flow methods (181,182).

IV. THEORETICAL DESCRIPTION OF THE NMR EXPERIMENTS

A. NMR of Noninteger Spin Quadrupolar Nuclei

Quadrupolar nuclei compose the majority of the magnetically active nuclei, of which the noninteger spin nuclei are the most numerous. NMR spectroscopy of these nuclei differs from that of $I = 1/2$ nuclei in that spectra of these nuclei are typically influenced by the interaction between the electric quadrupole moment of the nucleus and the electric field gradient at the nuclear site caused by the surrounding atoms. Thus, the quadrupolar interaction contains chemical information concerning the local environment of the nucleus and may be used to distinguish between, for example, different sodium cation sites in X and Y zeolites.

This quadrupolar interaction can sometimes be so large that observation of the nucleus is extremely difficult with NMR methods (e.g., for ^{35}Cl, ^{63}Cu, ^{127}I, etc.). In this case, nuclear quadrupole resonance (NQR) spectroscopy may be a more appropriate technique with which to study these nuclei. However, for many nuclei encountered in the characterization of zeolites or molecular sieves (e.g., ^{7}Li, ^{11}B, ^{17}O, ^{23}Na, ^{27}Al, ^{51}V, ^{133}Cs), the quadrupolar interaction is often sufficiently small that many of the NMR experiments used to study $I = 1/2$ nuclei can be applied. The central transition (m = |+1/2> to |−1/2>; see below) for noninteger spin quadrupolar nuclei is not broadened to first order by the quadrupolar interaction, and relatively narrow resonances may be observed. The presence of the outer satellite transitions is often ignored, and the noninteger spin is treated as a so-called fictitious spin-half system. The validity of this assumption will depend on both experimental parameters and the sample. There are a variety of consequences that result from the presence of these outer transitions, with different practical implications for obtaining quantitative spectra of zeolites. Acquiring NMR spectra of these nuclei requires an understanding of some of the underlying theory, so that the experimentalist is aware of the limitations of the method or to assure that the spectra obtained are quantitative. For this reason, the theory describing NMR experiments involving these nuclei will be provided below. For more detailed reviews of the theory of NMR of noninteger spin nuclei, the reader is referred to reviews by, for example, Freude and Haase (45) and Vega (in the *Encyclopedia of NMR*) (183).

1. First-Order Quadrupolar Interaction

The Hamiltonian for a quadrupolar nucleus in a magnetic field, with quadrupole moment Q, is a sum of the Zeeman and quadrupolar terms:

$$H = \omega_L I_z + H_Q \tag{4}$$

where Eq. (4) is written in frequency units. Standard symbols for frequencies are used throughout, where ω, ν, and δ denote frequencies expressed in radians, Hz, and ppm, respectively. The first-order quadrupolar interaction, $H_{Q(1)}$, is given by:

$$H_{Q(1)} = (1/2)Q'(\theta,\phi)\{I_z^2 - I(I+1)/3\} \quad (5)$$

where Q', the quadrupolar splitting, is a function of θ and ϕ, the polar angles that define the orientation of the principal axis system of the quadrupole tensor (defined by the principal components, V_{xx}, V_{yy}, and V_{zz}) in the Zeeman field (or laboratory frame) (Fig. 14) and the asymmetry parameter, η, [$\eta = (V_{xx}\text{-}V_{yy})/V_{zz}$]:

$$Q'(\theta,\phi) = (\omega_Q/2)[(3\cos^2\theta - 1) - \eta\sin^2\theta\cos 2\phi] \quad (6)$$

ω_Q, the quadrupole frequency, depends on the quadrupole coupling constant (QCC), e^2qQ/h (or C_Q in some texts):

$$\omega_Q = 3e^2qQ/[2I(2I-1)h] \quad (7)$$

(where $eq = V_{zz}$). Note that the QCC is zero for a nucleus located at a site with cubic, octahedral, or tetrahedral point group symmetry. The energy levels of the quadrupolar nucleus, E_m, in the Zeeman field are given by:

$$E_m = m_I\omega_L + Q'(\theta,\phi)\{m_I^2 - I(I+1)/3\}2 \quad (8)$$

The spectrum of a single crystal is split by the quadrupolar interaction, to first order, into 2I evenly spaced resonances with splittings, given by Q', and intensities that are proportional to:

$$< m_I \mid I_X \mid m_I + 1 >^2 = \{I(I+1) - m_I(m_I+1)\}/4 \quad (9)$$

Thus, when $\theta = 0°$ and the principal axis of the EFG tensor is aligned along the static magnetic field, the quadrupole splitting $Q'(0,\phi)$ is given by ω_Q. When $\theta = 90°$ and $\eta = 0$, $Q'(0,\phi) = -\omega_Q/2$.

One of the most important consequences that follows from Eq. (6) for noninteger spins is that the frequency of the $m = 1/2$ to $m = -1/2$, or central transition, does not depend on Q' and

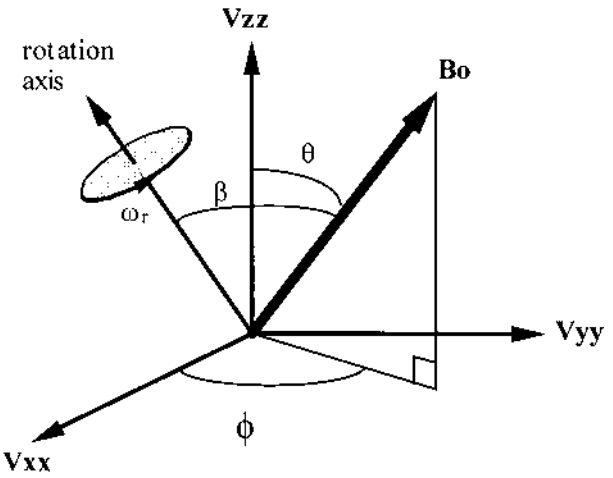

Fig. 14 The angles that define the orientation of the quadrupole tensor (V_{xx}, V_{yy}, V_{zz}) and the rotor axis, with respect to the static magnetic field, B_0.

is therefore unaffected to first order by the quadrupolar interaction. The outer, or satellite, transitions occur at $\pm Q$', $\pm 2Q$', etc., where Q' varies between ω_Q and $-\omega_Q/2$, depending on the orientation of the quadrupole tensor in the magnetic field. For a powder, characteristic lineshapes are observed, from which the QCC and η can be extracted. In practice, however, it is difficult to excite the whole spectrum with a single pulse for large QCCs. If necessary, spectra can be acquired at different resonance offsets, and the different spectra combined, taking into account effects such as the finite pulse width and the bandwidth of the probe, which both result in a reduction of the signal at large frequency offsets. [There is considerable inconsistency in the notation used in this field, and so some care is required in reading papers in this field. In some texts, the symbol $\omega_Q(\theta,\phi)$ is used for the quadrupole splitting and is a variable. In others, ω_Q is used to denote $(1/2)Q'(0,\phi)$ and represents the principal component of the quadrupole interaction.]

The first-order quadrupolar interaction can be averaged by MAS and the broad resonances from the satellite transitions are split into evenly spaced sidebands, separated by the spinning speed, that can spread over many kilohertz or megahertz. The isotropic resonance, or center band, is a sum of the central transition resonance, and the center bands of the $(2I - 1)$ satellite transitions. Quadupolar lineshapes for spinning at finite speeds have been calculated, and QCCs and η can be extracted from the simulations of the experimental spectra (184,185).

2. Second-Order Quadrupolar Interaction

A quadrupolar nucleus (with QCC > 0) does not align exactly along the static magnetic field (B_0), but along a field that is a combination of the static and quadrupolar fields (i.e., the quadrupolar nucleus is no longer quantized along B_0). Since the standard spin states $|m\rangle$ ($|\pm 3/2\rangle$, $|\pm 1/2\rangle$, etc.) used in NMR are those for nuclei quantized along B_0, off-diagonal elements (i.e., terms that do not commute with I_Z) appear in the Hamiltonian, H_Q. These terms can be ignored to first order and Eq. (5) results. For large QCCs, these terms have to be considered, and the full Hamiltonian is required:

$$H_Q = (1/6)\omega_Q\{3I_z^2 - I(I+1) + \eta(I_x^2 - I_y^2)\} \tag{10}$$

Second-order perturbation theory can be used to calculate the second-order correction to the energy levels, $\omega_Q^{(2)}$, which is proportional to ω_Q^2/ω_L. Hence, $\omega_Q^{(2)}$ *decreases* at higher fields. The powder lineshapes that result from the second-order energy shifts have been calculated and are discussed in detail in many reviews and papers (45,183). For example, for $I = 3/2$, the second-order correction to the frequency of the central transition is given by:

$$\omega_Q^{(2)} = -(3\omega_Q^2/16\omega_L)(1 - \cos^2\theta)(9\cos^2\theta - 1) \tag{11}$$

when $\eta = 0$. The important implication of Eq. (11) is that higher resolution spectra of quadrupolar nuclei may be obtained at higher fields. This is particularly important for the ^{17}O spectra of zeolites, where QCCs of 3–5.5 MHz, and thus broad resonances, are observed at low fields. The analysis of the one-pulse ^{23}Na MAS NMR spectra of NaY and NaX zeolites actually becomes more difficult at higher fields, due to a reduction in $\omega_Q^{(2)}$ and increased overlap of the resonances due to the different cation sites.

3. Magic Angle Spinning

Unlike the first-order term of the quadrupolar interaction, the second-order term is no longer a second-rank tensor and is not averaged to zero by MAS. This can be seen by expressing $\omega_Q^{(2)}$ in

terms of the zero-, second-, and fourth-order Legendre polynomials $P_n(\cos\theta)$, where $n = 0$, 2, and 4, respectively:

$$P_2(\cos\theta) = (3\cos^2\theta - 1)$$
$$P_4(\cos\theta) = (35\cos^4\theta - 30\cos^2\theta + 3) \quad (12)$$

A second-rank tensor contains terms with $n = 0$ and 2 only; the $n = 0$ terms are the isotropic terms (i.e., they do not vary as a function of the orientation in the magnetic field). Sufficiently fast spinning at an angle θ, such that $3\cos^2\theta - 1 = 0$ (the "magic angle"), averages the $P_2(\cos\theta)$ terms to zero. The averaged value for $\omega_Q^{(2)}$ under sample rotation, $<\omega_Q^{(2)}>_{rot}$, is given by:

$$<\omega_Q^2>_{rot} = A_0 + A_2P_2(\cos\beta) + A_4P_4(\cos\beta) \quad (13)$$

where A_0 is the isotropic shift, and A_2 and A_4 are functions of ωQ, ωL, η, and the relative orientation of the quadrupolar tensor and rotor axis. β is the angle between the rotor axis and the static magnetic field (see Fig. 14). $P_2(\cos\beta)$ and $P_4(\cos\beta)$ are averaged to zero and $-7/18$, respectively, for sample rotation at the magic angle. Thus, MAS only reduces the linewidths of the resonances obtained from powdered samples by approximately one-third, and for large QCCs significant second-order quadrupolar line broadening remains. Characteristic lineshapes are observed from which the QCC and η can be extracted (46,183,186). Examples of this are found in the ^{23}Na MAS NMR spectra of sodium-exchanged zeolites (Fig. 7) (109) and in the ^{11}B MAS NMR of boron-exchanged zeolites (61).

A shift in the center of gravity of the resonance to lower frequencies also occurs. This is called the second-order quadrupolar shift and is given by A_0 (or $\omega_{Q\text{iso}}^{(2)}$):

$$A_0 = \omega_{Q\text{iso}}^{(2)} = -(I(I+1) - 3/4)(1 + \eta^2/3)\omega_Q^2/30\omega_L \quad (14)$$

$\omega_{Q\text{iso}}^{(2)}$ depends on the Larmor frequency, and it is sometimes necessary to acquire spectra at more than one magnetic field, before the chemical shift, δ_{CS}, and $\omega_{Q\text{iso}}^{(2)}$ can be separated. Note that $\omega_{Q\text{iso}}^{(2)}$ is the value for the shift in radians. The shift in units of ppm, $\delta^{(2)}$, can be calculated ($\delta^{(2)} = 10^6 \times \omega_{Q\text{iso}}^{(2)}/\omega_L$). The quadrupolar shift can shift resonances out of the typical chemical shift ranges observed for different environments. This is particularly important for ^{27}Al NMR, where a large QCC can, for example, shift the resonance of a tetrahedrally coordinated aluminum atom into the chemical shift range typically observed for five- and six-coordinated aluminum atoms. This has complicated the interpretation of, for example, extraframework aluminum sites in zeolites.

The second-order broadening can sometimes be so large that the central transition resonances are no longer detected under conditions of MAS or are only observable as broad humps in the baseline. These spins are often termed "invisible." It is sometimes difficult to distinguish between these broad components and any baseline distortions that may be present. It is especially difficult when a range of QCCs is present and no sharp discontinuities are visible in the second-order quadrupolar lineshapes; this is often the case in the ^{27}Al MAS NMR spectra of the extraframework aluminum species or Brønsted acid sites in dehydrated zeolites. In addition, when narrower resonances are also present, the sidebands from these resonances may spread out over many ppm, making quantification of the broad humps extremely difficult.

4. Removing the Second-Order Quadrupolar Broadening

There are now four major approaches to reducing or removing the second-order quadrupolar broadening. The most straightforward approach is to work at as high fields as possible, since the broadening is inversely proportional to ωL. Two other approaches involve mechanical averaging of the second-order broadening [DAS (83) and DOR (82)]. The most recent technique, MQMAS (48,49), makes use of the different second-order

quadrupolar broadenings of the single and triple or five-quantum transitions to accomplish the averaging.

a. DOR

Averaging of the second-order quadrupolar broadening can be achieved by simultaneous spinning at two angles (82,83). These angles, β_1 and β_2, are chosen such that both the second- and fourth-order Legendre polynomials are reduced to zero:

$$\begin{aligned} &P_2(\cos\ \beta_1) = 0 \quad \beta_1 = \text{arc}\ \cos(1/3^{1/2})\ \text{(the ``magic angle'')} \\ &P_4(\cos\ \beta_2) = 0 \quad \beta_2 = 30.55 \text{ or } 70.12^\circ \end{aligned} \tag{15}$$

In practice, this achieved with a small rotor containing the sample (the inner rotor), which spins inside another rotor (the outer rotor). The axis of rotation of the inner rotor is inclined at angle of 30.55° to the axis of rotation of the outer rotor. The outer rotor is then spun at the magic angle. The isotropic shift, δ, observed under conditions of DOR is a sum of the chemical shift, δ_{CS}, and the second-order quadrupolar shift, $\delta_{Q\text{iso}}{}^{(2)}$, defined in Eq. (14), (where $\delta_{Q\text{iso}}{}^{(2)} = \omega_{Q\text{iso}}{}^{(2)}/\omega L$), and is therefore field dependent. $\delta_{Q\text{iso}}{}^{(2)}$ must be determined independently (e.g., from studies at different fields) in order to obtain δ_{CS}. The field dependence of $\delta_{\text{Qiso}}{}^{(2)}$ can be exploited to separate resonances with similar values for δ_{CS} but with different QCCs.

A major limitation to the technique remains the spinning speed of the outer rotor: speeds of not more than 1.2 kHz are typically achieved, and the spectra often contain many overlapping resonances. However, rotor synchronization will eliminate half of the spinning sidebands (187). The poor filling factor of the coil also results in long acquisition times for low-sensitivity nuclei such as ^{17}O.

b. DAS

The DAS experiment works by spinning separately about two DAS complementary angles (83) such that the second-order quadrupolar broadening is of equal magnitude for the two angles, but opposite in sign. A two-dimensional experiment is performed wherein the spins are returned to the z direction to preserve the magnetization while the flip between the two angles is implemented. The evolution due to $\omega_Q{}^{(2)}$ is refocused when $t_1 = t_2$, and an echo forms. Data acquisition is started at the echo maximum at t_2. A Fourier transform along t_1 yields the isotropic resonance, and quadrupolar second-order lineshapes are obtained after a Fourier transform along t_2. The DAS complementary angles can be found by finding solutions to the two simultaneous equations:

$$\begin{aligned} &P_2(\cos\beta_1) + kP_2(\cos\ \beta_2) = 0 \\ &P_4(\cos\beta_1) + kP_4(\cos\ \beta_2) = 0 \end{aligned} \tag{16}$$

For example, when $k = 5$, $\beta_1 = 0^\circ$ and $\beta_2 = 63.32^\circ$. Thus, spinning first about $\beta_1 = 0^\circ$ and then about $\beta_2 = 63.32^\circ$ will produce an echo at $5t_1 = t_2$.

DAS is only effective for nuclei with sufficiently long spin-lattice relaxation times, so that significant magnetization is not lost during the time used to flip the rotor. In addition, DAS will not remove the homonuclear dipolar couplings. Spin exchange may occur during the flipping time, which will result in broadening of the DAS spectra. Since this is a two-dimensional experiment, the experiment times are typically longer than for DOR.

c. Multiple-Quantum MAS NMR

In addition to the central transition, all odd-order multiple-quantum (MQ) transitions of quadrupolar nuclei (i.e., $3Q$, $5Q$ etc.) are unaffected by the first-order quadrupolar interaction. These MQ transitions are not directly observable but can be observed indirectly if the MQ coherence is transferred back to the observable single ($1Q$) coherence (188). The MQ

transitions are affected to second order by the quadrupolar interaction, $\omega_Q^{(2)}$, by an amount that depends on the order of coherence. Both the A_2 and A_4 terms defined in Eq. (13) depend on the order of coherence. For example:

$$A_{4(1)}/A_{4(3)} = -54/42 \tag{17}$$

for $I = 3/2$, where $A_{4(1)}$ and $A_{4(3)}$ are the A_4 terms for the $1Q$ and $3Q$ coherences, respectively. Frydman et al. demonstrated that the dependence of $\omega_Q^{(2)}$ on coherence order could be exploited to average the second-order interaction (48) and thus developed the MQMAS experiment.

The experiment is performed under conditions of MAS, so that the $A_2P_2(\cos\beta)$ terms are averaged to zero. Averaging of the $A_4P_4(\cos\beta)$ terms is then achieved by allowing the spins to evolve for different time periods in the single and multiple quantum time dimensions, t_{1Q} and t_{MQ}, respectively, such that the A_4 terms average to zero, i.e., for $I = 3/2$, $t_{1Q}/t_{3Q} = 42/54$. The experiment can be considered analogous to DAS, except that now the averaging is achieved by allowing the spins to evolve in two different MQ coherences; the experiment is also performed in a similar fashion. A single pulse, ϕ_1, is used to excite the $3Q$ (or MQ) transition (Fig. 15), in the simplest form of this experiment. Appropriate phase cycling of ϕ_1 and ϕ_2 is used to select the order of MQ coherence (e.g., 3 or 5). The spins are allowed to evolve for t_1, whereupon the $3Q$ coherence is then converted to a $1Q$ coherence (i.e., observable magnetization). Echo formation occurs in the t_2 dimension, when the A_4 terms cancel. Performing the Fourier transform along the echo maximum as a function of t_1 provides a spectrum free from second-order quadrupolar broadening. A Fourier transform performed in a direction perpendicular to the echo provides the second-order lineshape. A shearing transformation can be applied to the data, $S(t_1, t_2)$, that rotates the two-dimensional free induction decay, so that the isotropic and anisotropic spectra are observed in F1 and F2, respectively, after the Fourier transform. The method is relatively straightforward to implement on a conventional MAS probe and does not require any additional hardware; thus, there have already been a considerable number of applications of this experiment to zeolites.

The $3Q$ coherence can be excited with the highest efficiency, and thus MQMAS experiments using this coherence are more widely used. Clearly, for $I = 3/2$ nuclei, this represents

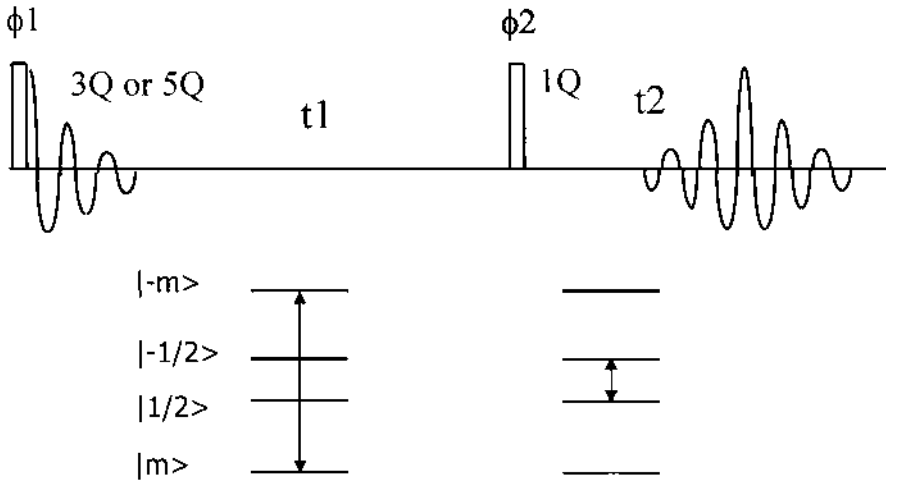

Fig. 15 The simplest variant of the MQMAS pulse sequence, showing the MQ (3Q or 5Q) and single-quantum coherences that evolve in t_1 and t_2, respectively.

the only MQ coherence. The triple-quantum nutation frequency is inversely proportional to the quadrupolar splitting, Q', and is given by $2\omega_1^3/3Q'^2$. Thus, the flip angle of the triple-quantum excitation pulse will depend on Q', and will not be constant for the whole powder, resulting in nonuniform excitation of the sample. Thus, the method is less successful for large QCCs (and, hence, larger values of Q'), especially at lower fields. However, even in these cases quantitative spectra may be obtained by using the parameters obtained from the MQMAS spectra to simulate the one pulse spectra, where the intensities are more readily quantified (Fig. 7).

Many variants of the initial MQMAS experiment have been developed that allow pure absorption spectra to be acquired in two dimensions [the shifted-echo (189,190), *z*-filter (191), and rotor synchronized *z*-filter (192) methods] and to improve the efficiency of the creation of MQ coherences, and their reconversion to 1*Q* coherences, by exciting a higher fraction of spins in the powder, such as the fast-amplitude modulation (FAM) shifted-pulse sequences developed by Vega et al. (193,194), and methods based on sweeping the rf offset [the double-frequency sweep sequence developed by Kentgens et al. (195,196)]. Some of these methods are compared in Ref. 197. The new sequences have been widely applied to study zeolites. For example, FAM pulses have been shown to improve the sensitivity of the ^{17}O MQMAS spectra of zeolites (198). Higher resolution spectra were obtained by using 5*Q*, as opposed to 3*Q*, sequences (198). However, the signal-to-noise ratio obtained with this sequence is much lower than that of the 3Q sequence, due to the lower efficiency of the 5*Q* excitation. The double-frequency sweep sequence was used to study dehydrated HZSM-5 (58).

5. Acquiring Spectra

Two extreme cases can be distinguished for single-pulse excitation at small resonant offsets, which depend on the relative magnitudes of the QCC and ω_1. When $\omega_1 >>$ QCC, the whole quadrupole spectrum is excited. In contrast, when QCC $>> \omega_1$, only the central transition is affected by ω_1. The transition can then be treated as an isolated or so-called fictitious spin-half transition. Unfortunately, the nutation frequency of the spins (i.e., the frequency with which the spins precess around the applied rf field) is different for these two cases. The signal intensity for $I = 3/2$ spins varies as 2 sin $\omega_1 t$ and sin $2\omega_1 t$ for $Q' = 0$ and $|Q'| >> \omega_1$, respectively, for a pulse of length t. The intensity of a resonance is thus dependent on Q' (Fig. 16). In many cases, the

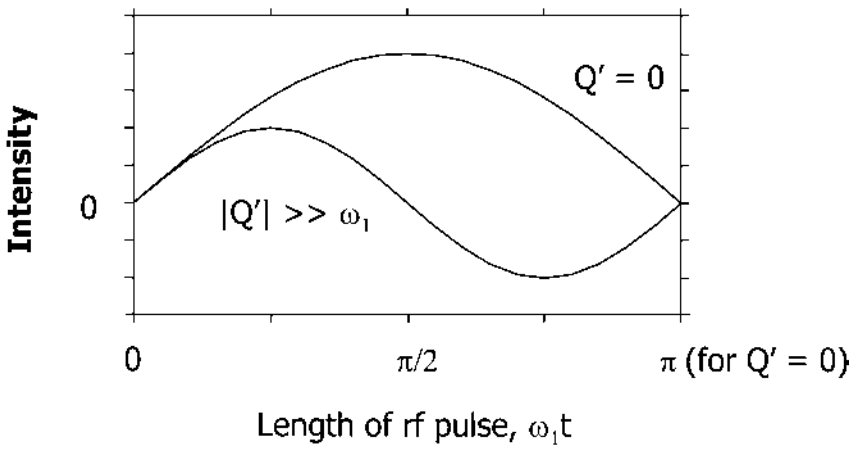

Fig. 16 The signal intensity versus pulse length for zero and a large quadrupolar spitting, Q'. The $\pi/2$ and π pulse lengths for $Q' = 0$ are shown.

QCC is of the same order as ω_1 (the intermediate regime). The orientation dependence of Q' then results in a spread of nutation frequencies, which can vary from ω_1 to $2\omega_1$ for $I = 3/2$. The second-order quadrupolar lineshape is also distorted, since the powder is no longer uniformly excited. The situation is more complex under MAS as Q' is partially averaged during the pulse, and Q' appears smaller (199). Thus, the nutation frequency will also depend on the spinning speed. Since $\sin 2\theta \approx 2 \sin\theta$ for small flip angles, θ, quantitative spectra and undistorted lineshapes can be obtained with short excitation pulses. This can be seen in Fig. 16, where the signal intensity obtained for large QCCs and $Q = 0$ can be seen to be very close, if pulses of 15° or less are used. More generally, the nutation frequencies for all noninteger spins vary between $\sin(I + 1/2)\omega_1 t$ and $(I + 1/2)\omega_1 t$ for $|Q'| << \omega_1$ and $|Q'| >> \omega_1$, respectively, and quantitative spectra can similarly be obtained with short flip angles. The spread in nutation frequencies obtained in the intermediate regime can be used to determine the QCC and η; this is the basis of nutation spectroscopy (200,201), which has been used to study sodium sites in zeolites (202).

6. Spin Counting

Since it is sometimes difficult to observe all of the spins in the sample, it is important to be able to estimate the number of spins that are actually observed. Without accurate spin counting, it is not always clear whether the species observed in the NMR spectra are representative of the whole sample, or whether they comprise a small subset of the spins that are present in the least distorted local environments. This is particularly important when obtaining ^{27}Al NMR spectra of dehydrated zeolites, where a large fraction of the sample is not always detected. Careful spin counting has also been shown to be important in ^{23}Na NMR. For example, in the assignment of the ^{23}Na spectra of faujasite zeolites, the concentrations of the different extraframework cation sites were shown to be very close to those obtained from diffraction data, after the intensities were scaled to account for the differences in the QCCs of the different sites (203).

Typically, spin counting is performed by comparing the intensity of the isotropic resonance in a spectrum of a sample of known weight, with the intensity from a standard sample whose spectrum was acquired under identical conditions. The theoretical intensity of each of the transitions can be calculated from Eq. (9) and will depend on I. Those for the central transition are shown in Table 3. Unfortunately, the total number of spins that contribute to the isotropic resonance will depend on the QCC. Three regimes can be identified:

(i) $\omega_Q = 0$

This will be the case, for example, in liquids, for nuclei in sites with cubic site symmetry, or for mobile species (e.g., hydrated cations in molecular sieves). In this case, all transitions

Table 3 Intensity of Central Transition of a Noninteger Spin Quadrupolar Nucleus as a Percentage of Total Intensity

Spin	Intensity (%)
3/2	40
5/2	26
7/2	19
9/2	15

will be excited, and the center band, in the absence of other anisotropic interactions, will contain intensity from 100% of the spins.

(ii) $0 < \omega_Q^2 < \omega_L\omega_r$

This is typically the case for ^{23}Na and ^{7}Li. Spinning sidebands from the satellite transitions are now visible, and the contribution of these satellites to the isotropic resonance needs to be estimated. Since the spinning speed is greater than the static linewidth of the central transition (as $\omega_Q^2/\omega_L\omega_r < 1$), the contribution to the intensity of the spinning sidebands from the central transition will be small, and can often be ignored. Note that other interactions, such as the CSA or dipolar coupling, may result in intensity in the sidebands. Fast spinning will clearly increase the intensity of the central transition in the center band (i.e., isotropic resonance) but will also increase the contribution of the satellites to the center band. Both contributions can be conveniently estimated with the graphical method proposed by Massiot et al. (204) or by simulation. The sideband intensities from the satellite transitions are often fairly constant close to the center band, allowing the contribution to the center band to be estimated from the intensity of other nearby sidebands. Having obtained the absolute intensity of the central transition resonance, the total number of spins in the sample can then be calculated from Table 3.

(iii) $\omega_r << \omega_Q$

The contribution of the outer satellites to the center band can be considered negligible when ω_Q is two or more orders of magnitude greater than ω_r. This is often the case for ^{27}Al NMR. In some cases, the outer satellites are not even observed due to poor setting of the magic angle, insufficient signal-to-noise, or ionic motion of the nucleus. However, a significant concentration of the central transition may now be present in the sidebands. This may be accounted for by integration of the whole resonance, including sidebands (if interference from the outer satellites is not a problem). In instances where outer satellites are observed, it is often easier to use the graphical method of Massiot et al. or to simulate the spectra.

7. Cross-polarization of Noninteger Spin Nuclei

Cross-polarization from an abundant $I = 1/2$ spin such as ^{1}H or ^{19}F to a quadrupolar nucleus, S, is accomplished by matching the nutation frequencies of the two spins I and S (the Hartmann-Hahn condition) during the contact time of the cross-polarization experiment (Fig. 2). As discussed earlier, the nutation frequency of noninteger spins depends on Q', and two different Hartmann-Hahn conditions apply for large and small Q':

$$\begin{aligned} &\text{(a)} \quad \omega_{1S} &&= \omega_{1I} \quad (|Q'| << \omega_{1S}) \\ &\text{(b)} \quad (S+1/2)\omega_{1S} &&= \omega_{1I} \quad (|Q'| >> \omega_{1S}) \end{aligned} \tag{18}$$

As for single-pulse excitation, case a applies when the whole quadrupole spectrum is excited, whereas case b applies when the isolated fictitious spin-1/2 system is excited. In the intermediate regime, $|Q'| \approx \omega_{1S}$, and a range of nutation frequencies is observed; thus, the Hartmann-Hahn condition is poorly defined in this regime.

Continuous on- or close-to-resonance irradiation (i.e., the spin-locking fields) is applied to both nuclei during the contact time. The outer satellite transitions for large QCCs (i.e., case b) are unaffected by the rf field, ω_1, in the absence of MAS, and S-spin magnetization buildup occurs along the direction of the spin-locking field for the central transition coherence only. Additional complications arise under conditions of MAS, which may also result in inefficient

CP (54,205,206). These arise from the time dependence in Q' introduced by the sample spinning. $Q'(t)$ depends on the orientation of the quadrupolar tensor (V_{xx}, V_{yy}, V_{zz}) with respect to the static magnetic field (defined by the polar angles θ and ϕ). This orientation varies continuously under MAS and $Q'(t)$ oscillates between positive and negative values (Fig. 17), with Q' crossing through zero two or four times per rotor period, depending on the relative orientation of the quadrupolar tensor and the rotor axis (the zero crossings).

A clearer understanding of the effect of MAS can be obtained by considering Fig. 17b, which shows a plot of the eigenvalues and eigenstates of an $I = 3/2$ nucleus as a function of Q' for close-to-resonance irradiation. For large values of $|Q'|$ the eigenstates are given by {|1/2> $\pm$ |−1/2>} and |±3/2>, and spins present in these states are said to be spin locked. Under MAS, Q' varies continuously. Near the zero crossings of Q', ω_1 is greater than $|Q'|$, and the rf field induces transitions between *all* |*m*> Zeeman levels. A sweep from $-Q'$ to $+Q'$, for example, results in a smooth conversion of the central transition coherences {|1/2> $\pm$ |-1/2>} to the outer Zeeman levels |±3/2>. If this sweep is performed sufficiently slowly (i.e., is adiabatic), all of the spins that populate the central transition coherences {|1/2> $\pm$ |−1/2>} are transferred to the |±3/2> states. Similarly, the populations in the |±3/2> states are transferred to the central transition coherences. In contrast, a very fast sweep will leave the

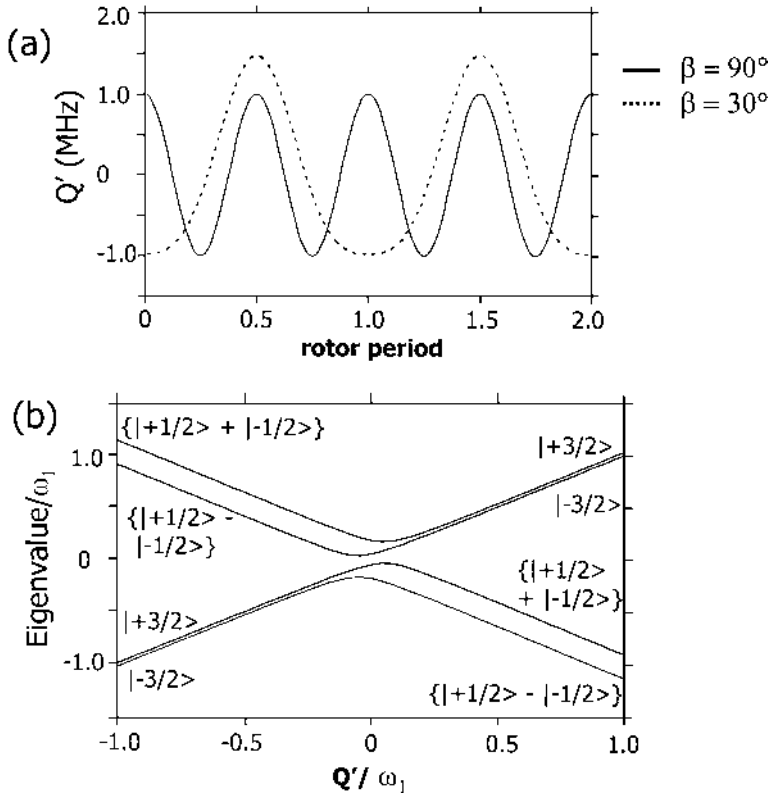

Fig. 17 (a) Plots of the variation of Q' as a function of time in the rotor period, for $\omega_Q = 1$ MHz, and two different values of β; $\eta = 0$ and the initial orientation of the quadrupolar tensor at time = 0 is chosen such that the rotation axis, B_0 and V_{zz} all lie in the same plane. (b) The eigenvalues for an $I = 3/2$ nucleus as a function of Q', for close to on-resonance irradiation. The eigenstates for large Q' are marked.

populations unchanged in their original states. A sweep performed at some intermediate rate will result in the transfer of populations into non-spin-locked coherences. Magnetization associated with these coherences decays rapidly. An adiabaticity parameter for the zero crossing, α', can be defined for a powder (206), which gives a measure of the efficiency of the population transfers:

$$\alpha' = \omega_1^2/\omega_r\omega_Q \tag{19}$$

Fast, intermediate, and adiabatic passages occur for $\alpha' << 1$, $\alpha' \approx 0.4$, and $\alpha' > 1$, respectively.

Magnetization builds up in one of the spin-locked coherences $\{|1/2> \pm |-1/2>\}$, during the spin-locking period of the CP experiment, assuming the Hartmann-Hahn condition is adequately matched. Under MAS, however, the magnetization will not necessarily remain in this coherence. Very slow MAS (i.e., adiabatic passages) results in the transfer of the magnetization into the $|\pm 3/2>$ states at the zero crossings for Q'. At the next zero crossing, all of the magnetization returns to the $\{|1/2> \pm |-1/2>\}$ and no magnetization is lost. This will be the case at the end of a rotor period, where an even number of crossings will have occurred. CP for values of α' in the intermediate regime will result in a rapid decay of the spin-locked magnetization, and inefficient or no CP. Fast MAS will leave the magnetization associated with the $\{|1/2> \pm |-1/2>\}$ coherence unaffected, and CP will again be efficient. The effect of MAS on the spin-locked magnetization has been demonstrated experimentally by Vega (205).

In conclusion, obtaining CP spectra of noninteger spin nuclei is not necessarily straightforward, even if the Hartmann-Hahn condition is matched. As a result, the inability to transfer magnetization from $I = 1/2$ to quadrupolar S spins does not necessarily indicate that the S spins are not dipolar-coupled to the I spins, but the converse (i.e., the detection of S-spin magnetization) can be used to demonstrate the proximity of S and I spins. It is relatively straightforward to calculate α' and to determine the conditions required for efficient CP. In general, it is easier to perform the experiment in the fast regime ($\alpha' << 1$), and $^{19}F/^{23}Na$ and $^{31}P/^{27}Al$ experiments have been performed, e.g., to characterize gas binding and zeolite structure under these conditions (88,100,168). The passages between Zeeman levels have also been shown to be important in the CP/DOR experiments (207) and in double-resonance experiments such as TRAPDOR and REAPDOR (see below) (54,96,208). For a fuller description of the effect of adiabatic passages on spin locking and CP, the reader is referred to the two papers by Vega (205,206).

B. Double-Resonance and Two-Dimensional NMR Experiments for Structure Elucidation

The information that can be obtained from the NMR experiment can be considerably enhanced if the interactions that exist between the NMR nuclei of interest and other, nearby NMR spins (i.e., NMR-active nuclei) can be exploited. These interactions can be used either to probe connectivity (i.e., establish that chemical bonds are present) or to measure the distances between atoms. The methods can be used to help develop three-dimensional models of the zeolite structure so as to determine where molecules bind in zeolites or, at the simplest level, to aid in the assignment of NMR resonances. If the experiment can be performed in a two-dimensional fashion, it is often possible to establish connectivities between different atoms *simultaneously*, sometimes allowing structural models for, say, the whole zeolite framework to be obtained in a single experiment.

The experiments can be divided into two main categories. In the first set of experiments, connectivity or distances between different types of nuclei (e.g., ^{29}Si and ^{27}Al) are probed. These exploit heteronuclear couplings between nuclei and are often referred to as

"double-resonance" experiments, since the experiments require that rf pulses be applied, often simultaneously, to both sets of nuclei. In the second set, "homonuclear" couplings between the same types of nuclei (e.g., between two different ^{29}Si nuclei in two different zeolite framework sites) are measured. Both the heteronuclear and homonuclear experiments may then be further divided into two categories, depending on the type of interaction that couples the two sets of nuclei. One class of experiments exploits the J-coupling interaction and requires that the nuclei of interest are separated by typically one or two chemical bonds. The J coupling is an example of a "through-bond" interaction, since it is a measure of the coupling between two nuclei, mediated via the intervening atomic (or molecular) orbitals. Experiments based on this interaction can, therefore, be used to measure connectivity. The size of the J coupling typically decreases extremely rapidly as a function of the number of bonds between the nuclei (unless extended π systems are present) limiting the length scales that can be probed with this method. Two nearby nuclei are also coupled by the "through-space" dipolar coupling interaction. This interaction is typically much larger than the J coupling (particularly for two- or three-bond J coupling) but, unlike the (isotropic part) of the J-coupling interaction, it is removed by MAS. Experiments have, however, been designed to reintroduce this interaction under MAS (see below). Since the size of this interaction is proportional to $1/r^3$, (Fig. 18) where r is the internuclear separation between the two spins, the internuclear distances between two atoms may be directly extracted from a measurement of the dipolar coupling the between the two nuclei. The dipolar experiments are complementary to those that exploit J coupling because the measurement of a short internuclear distance does not necessarily indicate that a chemical bond(s) connects the two atoms under investigation.

1. The Dipolar Interaction

Each nucleus creates its own local (magnetic) field in the presence of the larger external field (Fig. 18); nearby nuclei are affected by this field, which, depending on angle between the vector connecting the two spins and the direction of the static magnetic field (θ), can reduce or increase the total magnetic field felt by the nearby nucleus. This produces a shift of the NMR resonance to lower or higher frequency depending on θ, as can be seen from the expression for the dipolar coupling Hamiltonian between two different nuclei, I and S:

$$H_D = -D(3\cos\theta - 1)I_z S_z \tag{20}$$

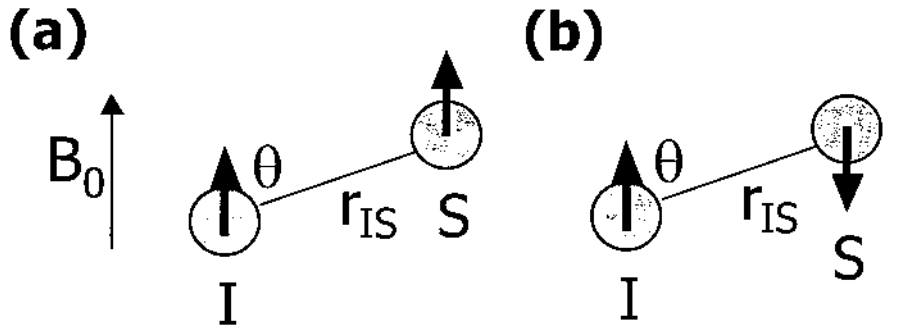

Fig. 18 The dipolar coupling interaction between two spin-1/2 nuclei, I and S. In (a), the I spin is coupled to the S |+1/2> state, while in (b), I is coupled to the |−1/2> state. The arrows on the two nuclei represent magnetization vectors oriented along the direction of the static magnetic field, B_0.

D is the dipolar coupling constant (in hertz) and is given by $\gamma_I\gamma_S h/2\pi r^3$. γ_I and γ_S are the gyromagnetic ratio of the I and S nuclei and h is Planck's constant. Thus, the dipolar coupling constants will be greatest and easiest to measure for coupling involving nearby nuclei with large values of γ (e.g., ^{1}H and ^{31}P). The operator I_zS_z in Eq. (20) indicates that the interaction involves a coupling between the I- and S-spin magnetization oriented along the direction of the static magnetic field (defined by convention as the z direction). The angular dependence of this interaction, $(3\cos\theta - 1)$, is *identical* to that observed earlier for the first-order quadrupolar interaction, when $\eta = 0$, i.e., the dipolar interaction can also be written in terms of a second-order Legendre polynomial, $P_2(\cos\theta)$. This holds true for all interactions that can be described by a second-rank tensor (e.g., chemical shift anisotropy).

2. Direct Measurements of Dipolar Couplings from the NMR Spectrum

The dipolar coupling between two sets of spin-1/2 nuclei (I and S) gives rise to a characteristic static spectrum for the powder (a so-called powder pattern) called a Pake doublet. The shape arises because each I spin has an essentially equal probability of being coupled to a "spin-up" or "spin-down" S spin (i.e., the S $|+1/2\rangle$ and $|-1/2\rangle$ states) (shown schematically in Fig. 18a and b). (Note the difference in spin populations between the $|+1/2\rangle$ and $|-1/2\rangle$ states is very small; nonetheless it is this difference in populations that gives rise to the small net magnetization that is detected in the NMR experiment in the sample coil.) As was discussed previously for the quadrupolar interaction, the dipolar coupling may also be removed by sufficiently fast MAS. Slow MAS will result in characteristic sideband patterns, which may be simulated to extract values for the dipolar coupling and hence the internuclear distance. For example, a ^{31}P-^{1}H dipolar-coupling constant of 17.5 kHz was measured by simulating the ^{1}H MAS NMR sidebands observed for deuterated TMP adsorbed on HY (151). The measured coupling constant is consistent with a distance of 1.4 Å and indicated that a transfer of the acidic protons from the framework to the sorbed probe molecule to form $TMPH^+$ had occurred. In practice, this approach tends only to be feasible for couplings involving directly bound atoms because the analysis of the sidebands becomes much less straightforward when additional anisotropic interactions of similar magnitudes need to be included in the simulation. For example, the spinning sidebands in the ^{31}P spectra of the same system could only be well reproduced in a simulation when the ^{31}P CSA of the $TMPH^+$ phosphorus atom was included (along with the dipolar coupling) in the simulation (209).

3. Experiments Designed to Measure Dipolar Coupling

A different approach needs to be taken to measure distances involving smaller dipolar couplings. The majority of these experiments are based on the SEDOR NMR experiment developed by Hahn et al. in the 1950s (Fig. 19) (210). The experiment is performed by applying a spin-echo experiment to one set of nuclei. In the normal spin-echo experiment, the magnetization evolves in the x-y plane, following the first $\pi/2$ pulse, under the influence of a number of interactions (e.g., the chemical shift and the dipolar coupling interactions). The π pulse applied at the end of the "evolution period" serves to refocus the magnetization and an echo is formed at the end of the "refocusing period." For example, magnetization represented by the operator I_y evolves under the dipolar Hamiltonian at a frequency given in angular units by $\omega_D = 2\pi D(3\cos\theta - 1)$ to produce the coherence represented by the operator I_xS_z. That is, the coherence I_xS_z, which now involves both the I and S spins, has been created by the dipolar coupling interaction. The magnetization appears to decay because different spins in the powdered sample are associated with different values of θ. A $(\pi)_y$ pulse applied to the I spins now converts the I_x term of the operator I_xI_z to $-I_x$, so that the overall term changes in sign.

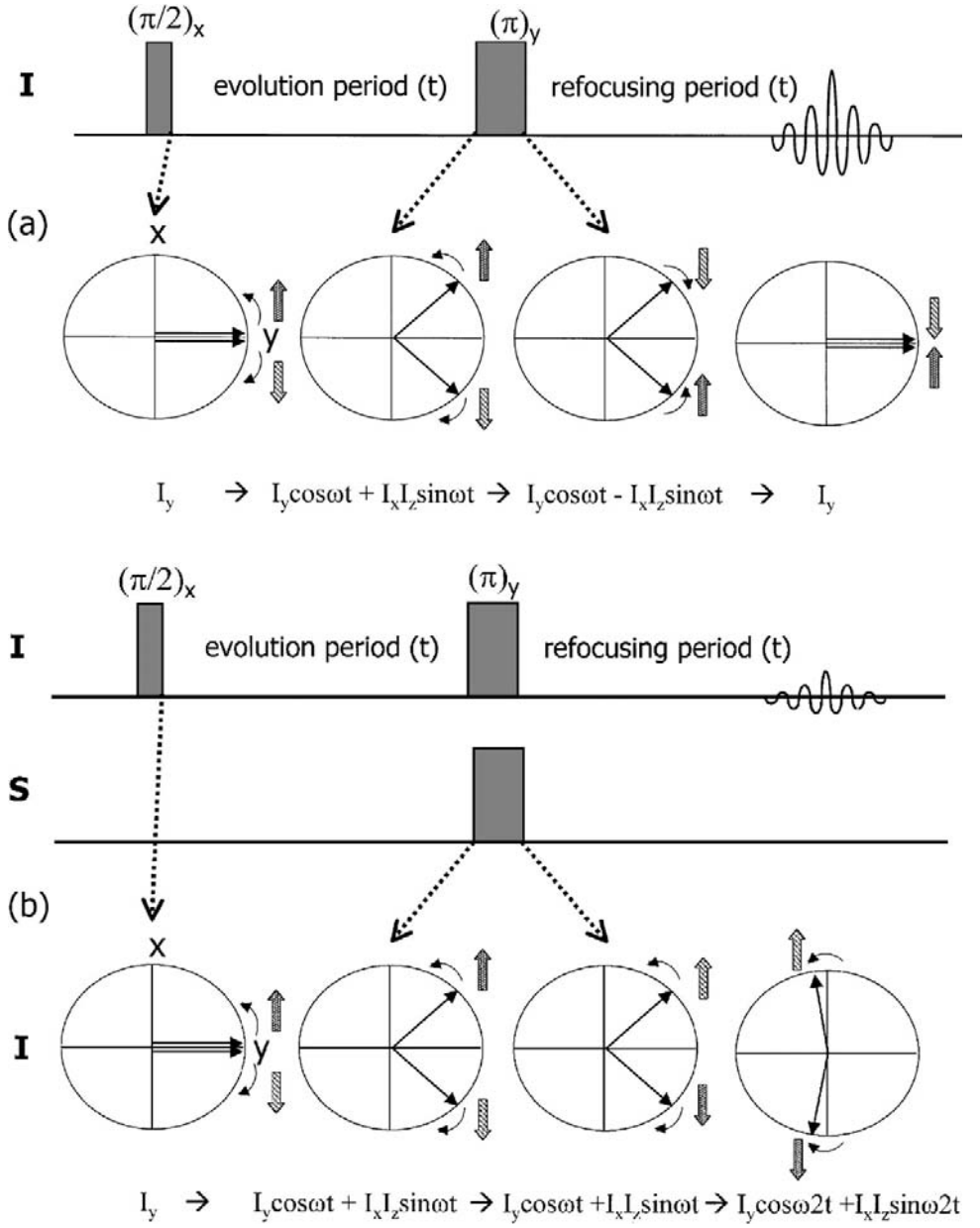

Fig. 19 The SEDOR experiment involving two sets of spins *I* and *S*. The spin-echo experiment is shown in (a), which serves as the control experiment. The double resonance experiment is shown in (b), where a π pulse is now applied to the *S*-spin channels.

The *I*-spin magnetization continues to evolve in the same direction, but the effect is now to refocus the magnetization to produce an echo. This is shown schematically in Fig. 19 by using both the operator and magnetization vector description.

The experiment is modified in the SEDOR experiment by simultaneously applying a second pulse simultaneously to the *S* spins. This π pulse now inverts the *S*-spin magnetization (which can be represented by S_z), i.e., $S_z \rightarrow -S_z$. Thus, the magnetization of the *I*-*S* coupled *I* spins continues to evolve in the same direction and appears to be unaffected by the application of the two π pulses, no longer refocusing to form an echo. Other *I* spins that are not coupled to nearby *S* spins will be refocused by the π pulses, forming an echo. The loss of intensity at the *I*-spin intensity at the echo is then measured as a function of the evolution time. The larger the dipolar coupling constant, the more rapidly the echo intensity decays, as the evolution period is increased. This effect can be readily calculated using expressions derived using the operator notation shown in Fig. 19 and the dipolar coupling constant extracted.

a. REDOR

The REDOR experiment is the MAS variant of the SEDOR experiment, as it is designed to reintroduce the dipolar coupling removed by the MAS (211). Since MAS works by refocusing the signal or magnetization every rotor period (i.e., when the rotor has made one complete evolution), π pulses are now introduced half-way through the rotor period to prevent the refocusing. In order to prevent the dephasing that has occurred in one rotor period from being refocused in the next rotor period, π pulses are also inserted at the end of every rotor period. For example, the ^{27}Al/^{31}P REDOR pulse sequence used to study the interaction with the base TMP with the zeolite framework is shown in Fig. 20. The ^{27}Al spins were monitored by applying short pulses to ensure that the whole solid sample was uniformly excited. This represents one of the three main REDOR pulse sequences; for more details, the reader is referred to two review articles (86,212). The TEDOR NMR experiment is a variant of the REDOR experiment that uses the REDOR pulse sequence to transfer magnetization from one set of coupled spins to the other, allowing the REDOR experiment to be performed in a two-dimensional fashion (213).

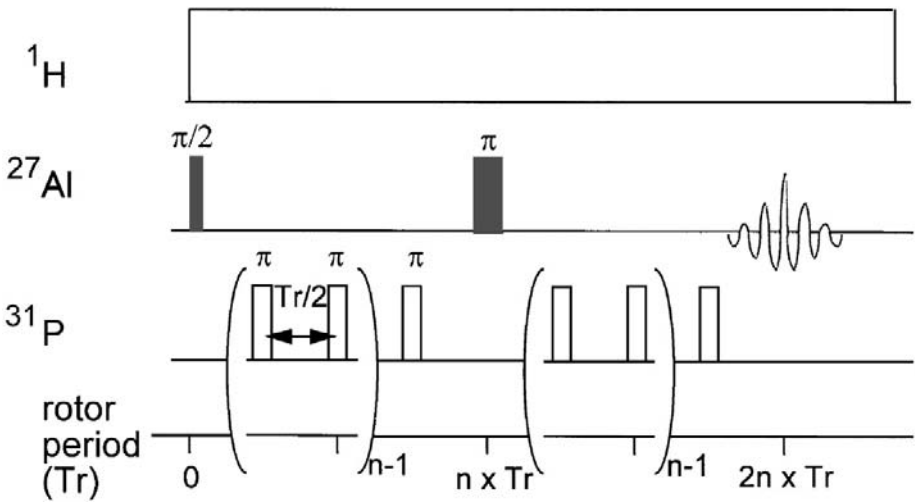

Fig. 20 The ^{27}Al/^{31}P REDOR NMR sequence. A spin echo is applied to the ^{27}Al spins, while π pulses are applied to the ^{31}P spins. ^{1}H decoupling may also be applied.

b. TRAPDOR (Transfer of Populations in Double-Resonance) NMR

This experiment is designed to measure dipolar coupling involving one (or more) quadrupolar nuclei, by making use of the population transfers (discussed in detail for the CP experiment) that occur between the Zeeman levels of a quadrupolar nucleus under conditions of slow MAS and continuous rf irradiation of the quadrupolar nucleus, *S* (54,55). For example, in $^{1}H/^{27}Al$ TRAPDOR NMR (Fig. 21), ^{27}Al irradiation is applied during the evolution period of the ^{1}H spin-echo experiment. The population transfers between the *S* spin (^{27}Al) Zeeman levels alter the evolution of the dipolar coupled $I = 1/2$ (^{1}H) magnetization and prevent refocusing of the ^{1}H magnetization at the spin echo, causing a TRAPDOR "effect." As in the REDOR and SEDOR experiment, the TRAPDOR fraction, defined as $(1 - I/I_0)$, where *I* and I_0 are the intensities at the spin echo with and without irradiation of the *S* spins, will depend on the dipolar coupling between spins: the greater the dipolar coupling, the greater the dephasing of the *I* spins, and thus the greater the TRAPDOR effect. Slower spinning ensures that the passages between the *S* spins are closer to being adiabatic, resulting in more efficient population transfers and a larger TRAPDOR fraction. Values of $\alpha' > 1$ [where α' was defined in Eq. (19)] ensure that most of the passages that occur for the whole powder sample are adiabatic, but even values for α' as low as 0.27 have been shown to give significant TRAPDOR dephasing in the $^{1}H/^{27}Al$ TRAPDOR experiment (55).

A TRAPDOR effect can only be determined if the *S*-spin irradiation frequency lies within the *S*-spin (e.g., ^{27}Al) first-order quadrupole spectrum. Thus, the size of the QCC for the quadrupolar nucleus, *S*, can be estimated by mapping out the intensity of the *I* echo, as a function of the *S* irradiation frequency offset, and determining where the TRAPDOR fraction drops to zero (55). For $I = 5/2$ nuclei, the edge of the first-order quadrupole spectrum occurs at $\pm 2\nu_Q = (3/10)$ QCC.

The TRAPDOR NMR experiment can be applied to probe internuclear distances in two situations where the REDOR NMR experiment may prove difficult. First, the TRAPDOR experiment can detect dipolar coupling to "invisible" spins. Second, the TRAPDOR experiment is designed to measure coupling involving quadrupolar nuclei, where it is not often possible to use a π pulse to excite the whole sample. The dipolar coupling measured in the TRAPDOR experiment is larger than that measured in the REDOR experiment because the TRAPDOR experiment probes the coupling to spins in all the Zeeman levels of the quadrupolar nucleus. Hence, the TRAPDOR experiment may be more sensitive to longer range dipolar couplings.

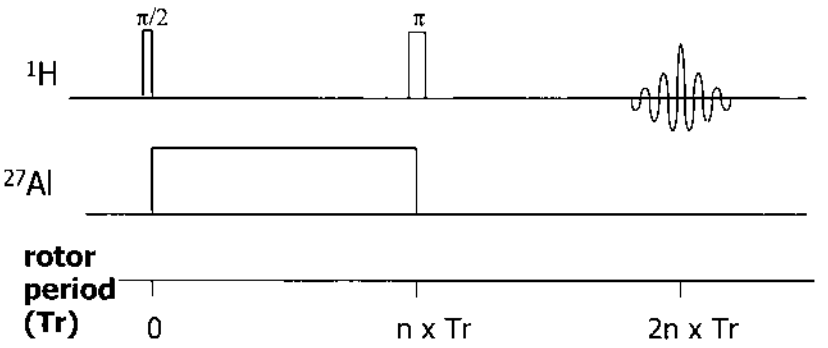

Fig. 21 The $^{1}H/^{27}Al$ TRAPDOR NMR pulse sequence. The intensities (at the echo) are determined with (*I*) and without (I_0) ^{27}Al irradiation.

c. REAPDOR (Rotational Echo and Adiabatic Passages Double Resonance) NMR

This experiment involves a combination of the TRAPDOR and REDOR methods (96). This experiment does not require multiple rotor periods of *S*-spin irradiation to detect weak *I-S* coupling (*cf.* TRAPDOR), and consequently the REAPDOR fractions are simpler to calculate (208). The REAPDOR dephasing is also less sensitive to the relative orientation between the QCC and dipolar tensors. Thus, this experiment typically yields more accurate internuclear distances than can be obtained from the TRAPDOR experiment.

4. Two-Dimensional NMR Studies of Framework Connectivities Based on J Coupling

The ability to resolve the different T sites in a zeolite framework allowed two-dimensional NMR experiments to be employed to probe the proximity between different sites. These two-dimensional experiments, and their one-dimensional variants, require a method or interaction that connects the different sites (or NMR-active nuclei). Experiments based on the J coupling have been most widely used to study zeolites (1). The basic ^{29}Si COSY and CP-COSY sequences are shown schematically below. The "(CP)" pulse length (the contact time) is optimized for maximal $^{1}H \rightarrow {}^{29}$Si polarization transfer.

$$\begin{aligned} &\text{COSY}: && ^{29}\text{Si}: && (\pi/2) - t_1 - (\pi/2) - t_2(\text{acq})..\\ &\text{CP}-\text{COSY} && ^{1}\text{H}: && (\pi/2)_x\ (\text{CP})_y\\ & && ^{29}\text{Si}: && \qquad (\text{CP}) - t_1 - (\pi/2) - t_2(\text{acq})..\end{aligned}$$

The Hamiltonian that describes the J-coupling interaction has the form $H_J = -2\pi J I_{1z} I_{2z}$, where I_1 and I_2 represent two different ^{29}Si nuclei that are coupled via J coupling of size J (measured in hertz). Thus the magnetization will evolve during the t_1 and t_2 periods under the Hamiltonian, H_J (and the Hamiltonians that describe the chemical shifts of the two nuclei). For example, the "*x-y*" magnetization due to the I_1 nucleus that is produced following an initial $(\pi/2)_x$ pulse (or via the CP sequence) (I_{1x} or I_{1y}) will evolve under H_J to form coherences represented by operators of the form $I_{1y}I_{2z}$. The second $\pi/2$ pulse will convert this coherence to $-I_{1z}I_{2y}$. This coherence then evolves in the t_2 period to produce observable I_2 spin magnetization (i.e., I_{2x}). Hence, this sequence converts I_1 spin magnetization to I_2 spin magnetization (and vice versa) for two sets of spins that are connected via the J coupling. This produces a cross-peak in the two-dimensional spectrum connecting resonances from the I_1 and I_2 spins. The INADEQUATE variant of the experiment has also been used to study zeolites (27,28,90). This is a less sensitive experiment since it involves the creation of double-quantum coherences. However, no "diagonal" peaks are seen in the two-dimensional experiment allowing coupling between spins with very similar (or identical) chemical shifts to be resolved.

V. CONCLUSIONS

This chapter has outlined many of the varied NMR experiments that have been applied to study zeolite structure, gas binding, and reactivity. Each experiment, particularly if combined with another technique, or a series of other NMR experiments, can result in extremely detailed chemical and/or structural information. New NMR experiments have permitted increasingly higher resolution spectra to be obtained, even in the presence of considerable disorder. By exploiting J or dipolar coupling, three-dimensional models of structure may be built up; these, coupled with diffraction experiments, are playing an increasingly important role in defining structure. Methods for studying catalytic reactions under increasingly realistic conditions have

been developed and continue to be improved. These can now be used to determine *in situ* the species inside the pores of the zeolites, information that is difficult to obtain directly from other methods. The types of information that can be obtained by NMR, and the role that NMR plays in characterizing zeolites, can be expected to increase.

ACKNOWLEDGMENTS

I thank current and former members of my research group who have contributed to much of what I have discussed in this chapter. Particular thanks go to Jennifer Readman, Hsien-Ming Kao, Haiming Liu, Kwang-Hun Lim, Michael Ciraolo, and Peter Chupas. The unpublished (^{17}O NMR) work discussed in this chapter was performed under the support of the Department of Energy, Basic Energy Sciences (DE-FG02-96ER14681). Alexander Vega is thanked for many helpful discussions and insightful comments over the last decade.

REFERENCES

1. CA Fyfe, Y Feng, H Grondey, GT Kokotailo, H Gies. Chem Rev 91:1525, 1991.
2. J Klinowski. Anal Chim Acta 283:929, 1993.
3. E Lippmaa, M Magi, A Samoson, G Engelhardt, AR Grimmer. J Am Chem Soc 102:4889, 1980.
4. E Lippmaa, M Magi, A Samoson, M Tarmak, G Engelhardt. J Am Chem Soc 103:4992, 1981.
5. J Klinowski, S Ramdas, JM Thomas, CA Fyfe, JS Hartman. J Chem Soc Faraday Trans II 78:1025, 1982.
6. JM Thomas, CA Fyfe, S Ramdas, J Klinowski, GC Gobbi. J Phys Chem 86:3061, 1982.
7. G Engelhardt, U Lohse, E Lippmaa, M Tarmak, M Magi. Z Anorg Allg Chem 478:239, 1981.
8. JM Thomas, J Klinowski, S Ramdas, BK Hunter, DTB Tennakoon. Chem Phys Lett 102:158, 1983.
9. JV Smith, CS Blackwell, GL Hovis. Nature 309:140, 1984.
10. JV Smith, CS Blackwell. Nature 303:223, 1983.
11. JB Higgins, DE Woessner. EOS Trans Am Geophys Union 63:1139, 1983.
12. R Radeglia, G Engelhardt. Chem Phys Lett 114:28, 1985.
13. S Ramdas, J Klinowski. Nature 308:521, 1984.
14. LM Bull, B Bussemer, T Anupold, A Reinhold, A Samoson, J Sauer, AK Cheetham, R Dupree. J Am Chem Soc 122:4948, 2000.
15. G Valerio, A Goursot, R Vetrivel, DR Salahub. Micropor Mesopor Mater 30:111, 1999.
16. G Valerio, A Goursot, R Vetrivel, O Malkina, V Malkin, DR Salahub. J Am Chem Soc 120:11426, 1998.
17. B Bussemer, KP Schroder, J Sauer. Solid State Nucl Magn Reson 9:155, 1997.
18. H Hamdan, B Sulikowski, J Klinowski. J Phys Chem 93:350, 1989.
19. EF Rakiewicz, KT Mueller, TP Jarvie, KJ Sutovich, TG Roberie, AW Peters. Micropor Mater 7:81, 1996.
20. CA Fyfe, GC Gobbi, J Klinowski, JM Thomas, S Ramdas. Nature 296:530, 1982.
21. CA Fyfe, H Strobl, GT Kokotailo, GJ Kennedy, GE Barlow. J Am Chem Soc 110:3373, 1988.
22. CA Fyfe, GJ Kennedy, CT DeSchutter, GT Kokotailo. J Chem Soc Chem Commun 541, 1984.
23. CA Fyfe, H Gies, Y Feng. J Am Chem Soc 111:7702, 1989.
24. CA Fyfe, H Gies, Y Feng, GT Kokotailo. Nature 341:223, 1989.
25. CA Fyfe, H Grondey, Y Feng, GT Kokotailo. J Am Chem Soc 112:8812, 1990.
26. CA Fyfe, Y Feng, H Gies, H Grondey, GT Kokotailo. J Am Chem Soc 112:3264, 1990.
27. CA Fyfe, Y Feng, H Grondey, GT Kokotailo, A Mar. J Phys Chem 95:3747, 1991.
28. CA Fyfe, H Grondey, Y Feng, GT Kokotailo, S Ernst, J Weitkamp. Zeolites 12:50, 1992.
29. CA Fyfe, H Gies, Y Feng. J Chem Soc Chem Commun 1240, 1989.
30. H Koller, A Wolker, LA Villaescusa, MJ Diaz-Cabanas, S Valencia, MA Camblor. J Am Chem Soc 121:3368, 1999.
31. DF Shantz, RF Lobo. Chem Mater 10:4015, 1998.

32. DF Shantz, RF Lobo. J Am Chem Soc 120:2482, 1998.
33. DF Shantz, RF Lobo. J Phys Chem B 103:5920, 1999.
34. DF Shantz, JS auf der Gunne, H Koller, RF Lobo. J Am Chem Soc 122:6659, 2000.
35. S-H Park, JB Parise, H Gies, H Liu, CP Grey, BH Toby. J Am Chem Soc 122:11023, 2000.
36. S-H Park, P Daniels, H Gies. Micropor Mesopor Mater 37:129, 2000.
37. HH Cho, SH Kim, YG Kim, YC Kim, H Koller, MA Camblor, SB Hong. Chem Mater 12:2292, 2000.
38. MA Camblor, ME Davis. J Phys Chem 98:13151, 1994.
39. MA Camblor, RF Lobo, H Koller, ME Davis. Chem Mater 6:2193, 1994.
40. GJ Johnson, PJ Mead, SE Dann, MT Weller. J Phys Chem 104:1454, 2000.
41. IL Moudrakovski, A Sayari, CI Ratcliffe, JA Ripmeester, KF Preston. J Phys Chem 98:10895, 1994.
42. A Sayari, I Moudrakovski, C Danumah, CI Ratcliffe, JA Ripmeester, KF Preston. J Phys Chem 99:16373, 1995.
43. A Labouriau, KC Ott, J Rau, WL Earl. J Phys Chem B 104:5890, 2000.
44. G Ricchiardi, J Sauer. Z Phys Chem-Int J Res Phys Chem Chem Phys 209:21, 1999.
45. D Freude, J Haase. In: NMR Basic Principles and Progress. Berlin: Springer-Verlag, 1993, Vol 29, p 1.
46. DR Corbin, RD Farlee, GD Stucky. Inorg Chem 23:2920, 1984.
47. MF Ciraolo, P. Norby, JC Hanson, DR Corbin, CP Grey. J Phys Chem B 103:346, 1999.
48. L Frydman, JS Harwood. J Am Chem Soc 117:5367, 1995.
49. A Medek, JS Harwood, L Frydman. J Am Chem Soc 117:12779, 1995.
50. C Fernandez, J-P Amoureux. Chem Phys Lett 242:449, 1995.
51. PR Bodart, JP Amoureux, M Pruski, A Bailly, C Fernandez. Magn Reson Chem 37:S69, 1999.
52. H Ernst, D Freude, I Wolf. Chem Phys Lett 212:588, 1993.
53. H Koller, EL Meijer, RA van Santen. Solid State NMR 9:165, 1997.
54. CP Grey, AJ Vega, WS Veeman. J Chem Phys 98:7711, 1993.
55. CP Grey, AJ Vega. J Am Chem Soc 117:8232, 1995.
56. H-M Kao, CP Grey. J Phys Chem 100:5105, 1996.
57. HM Kao, CP Grey. Chem Phys Lett 259:459, 1996.
58. APM Kentgens, D Iuga, M Kalwei, H Koller. J Am Chem Soc 123:2925, 2001.
59. CA Fyfe, JL Bretherton, LY Lam. J Am Chem Soc 123:5285, 2001.
60. SMC Menezes, VL Camorim, YL Lam, RAS San Gil, A Bailly, JP Amoureux. Appl Catal A 207:367, 2001.
61. C Fild, H Eckert, H Koller. Angew Chem 37:2505, 1998.
62. G Engelhardt, D Michel. High-Resolution Solid State NMR of Silicates and Zeolites. Chichester: John Wiley & Sons, 1987.
63. D Padro, AP Howes, ME Smith, R Dupree. Solid State NMR 15:231, 2000.
64. A Labouriau, WL Earl. Chem Phys Lett 270:278, 1997.
65. KFGJ Scholle, WS Veeman. Zeolites 5:118, 1985.
66. E Brunner, D Freude, M Hunger, H Pfeifer, W Reschetilowski, B Unger. Chem Phys Lett 148:226, 1988.
67. RF Lobo, ME Davis. J Am Chem Soc 117:3766, 1995.
68. C Fild, H Eckert, H Koller. J Am Chem Soc 122:12590, 2000.
69. C Fild, DF Shantz, RF Lobo, H Koller. Phys Chem Chem Phys 2:3091, 2000.
70. HKC Timken, E Oldfield. J Am Chem Soc 109:7669, 1987.
71. F Taulelle, A Samoson, T Loiseau, G Ferey. J Phys Chem B 102: 8588, 1998.
72. S-H Park, M Kleinsorge, CP Grey, JB Parise. J Solid State Chem 167:310, 2002.
73. OB Lapina, VM Mastikhin, AA Shubin, VN Krasilnikov, KI Zamaraev. Prog NMR Spectrosc 24:457, 1992.
74. S Dzwigaj, M Matsuoka, M Anpo, M Che. Catal Lett 72:211, 2001.
75. T Sen, PR Rajamohanan, S Ganapathy, S Sivasanker. J Catal 163:354, 1996.
76. Z Xu, JF Stebbins. Solid State NMR 11:243, 1998.

77. UT Pingel, JP Amoureux, T Anupold, F Bauer, H Ernst, C Fernandez, D Freude, A Samoson. Chem Phys Lett 294:345, 1998.
78. LM Bull, AK Cheetham, T Anupold, A Reinhold, A Samoson, J Sauer, B Bussemer, Y Lee, S Gann, J Shore, A Pines, R Dupree. J Am Chem Soc 120:3510, 1998.
79. JE Readman, M Ziliox, N Kim, CP Grey. Chem Commun 2808, 2002.
80. Z Xu, JF Stebbins. Geochim. Cosmochim Acta 62:1803, 1998.
81. Y Wu, BQ Sun, A Pines, A Samoson, E Lippmaa. J Magn Reson 89:297, 1990.
82. A Samoson, E Lippmaa, A Pines. Mol Phys 65:1013, 1988.
83. KT Mueller, BQ Sun, CG Chingas, JW Zwanziger, T Terao, A Pines. J Magn Reson 86:470, 1990.
84. AV Larin, DP Vercauteren. Int J Quantum Chem 82:182, 2001.
85. ERH van Eck, WS Veeman. Solid State NMR 1:1, 1992.
86. T Gullion, J Schaefer. Adv Magn Reson 13:57, 1989.
87. AW Hing, S Vega, J Schaefer. J Magn Reson 96:205, 1992.
88. CA Fyfe, KC Wongmoon, Y Huang, H Grondey, KT Mueller. J Phys Chem 99:8707, 1995.
89. CA Fyfe, KC Wong-Moon, Y Huang, H Grondey. J Am Chem Soc 117:10397, 1995.
90. CA Fyfe, DH Brouwer, AR Lewis, JM Chezeau. J Am Chem Soc 123:6882, 2001.
91. CA Fyfe, AR Lewis, JM Chézeau, H Grondey. J Am Chem Soc 119:12210, 1997.
92. NP Kenaston, AT Bell, JA Reimer. J Phys Chem 98:894, 1994.
93. SL Hu, JA Reimer, AT Bell. J Phys Chem B 101:1869, 1997.
94. HG Niessen, M Van Buskirk, C Dybowski, DR Corbin, JA Reimer, AT Bell. J Phys Chem 105:2945, 2001.
95. HM Kao, CP Grey, K. Pitchumani, PH Lakshminarasimhan, VJ Ramamurthy. Phys Chem A 102:5627, 1998.
96. T Gullion. J Magn Reson A 117:326, 1995.
97. S Ganapathy, S Vega. J Am Chem Soc 120:1078, 1998.
98. Y Ba, J He, CI Ratcliffe, JA Ripmeester. J Am Chem Soc 121:8387, 1999.
99. CA Fyfe, AR Lewis. J Phys Chem B 104:48, 2000.
100. KH Lim, CP Grey. J Chem Soc Chem Commun 2257, 1998.
101. KH Lim, F Jousse, S Auerbach, CP Grey. J Phys Chem 105:9818, 2001.
102. M Feuerstein, M Hunger, G Engelhardt, JP Amoureux. Solid State NMR 7:95, 1996.
103. R Jelinek, S Ozkar, HO Pastore, A Malaek, GA Ozin. J Am Chem Soc 115:563, 1993.
104. R Jelinek, A Malaek, GA Ozin. J Phys Chem 99:9236, 1995.
105. H Koller, AR Overweg, RAV Santen, JWD Haan. J Phys Chem 101:1754, 1997.
106. M Hunger, G Engelhardt, H Koller, J Weitkamp. Solid State NMR 2:111, 1993.
107. KN Hu, LP Hwang. Solid State NMR 12:211, 1998.
108. M Hunger, P Sarv, A Samoson. Solid State NMR 9:115, 1997.
109. KH Lim, CP Grey. J Am Chem Soc 122:9768, 2000.
110. S Caldarelli, A Bucholz, M Hunger. J Am Chem Soc 123:7118, 2001.
111. AN Fitch, H Jobic, A Renouprez. J Phys Chem 90:1311, 1986.
112. WJ Mortier. Compilation of Extraframework Sites in Zeolites. London: Butterworth-Heineman, 1982.
113. DH Olson. Zeolites 15:439, 1995.
114. WJ Mortier, EVD Bossche, JB Uytterhoeven. Zeolites 4:41, 1984.
115. G Engelhardt. Micropor Mater 12:369, 1997.
116. CP Grey, FI Poshni, AF Gualtieri, P Norby, JC Hanson, DR Corbin. J Am Chem Soc 119:1981, 1997.
117. CJ Jameson. In: J. Mason, ed. Multinuclear NMR. New York: Plenum, 1987, p 51.
118. H Koller, B Burger, AM Schneider, G Engelhardt, J Weitkamp. Micropor Mater. 5:219, 1995.
119. P Norby, FI Poshni, AF Gualtieri, JC Hanson, CP Grey. J Phys Chem B 102:839, 1998.
120. M Hunger, U Schenk, A Buchholz. J Phys Chem B 104:12230, 2000.
121. RJ Accardi, RF Lobo. Micropor Mesopor Mater 40:25, 2000.
122. M Feuerstein, RF Lobo. Chem Commun 1647, 1998.
123. M Feuerstein, RF Lobo. Solid State Ionics 118:135, 1999.

124. M Feuerstein, RJ Accardi, RJ Lobo. J Phys Chem B 104:10282, 2000.
125. J Plévert, LC de Ménorval, FD Renzo, F Fajula. J Phys Chem B 102:3412, 1998.
126. RJ Accardi, RF Lobo, M Kalwei. J Phys Chem B 105:5883, 2001.
127. H Liu, CP Grey. Micropor Mater 53:109, 2002.
128. MF Ciraolo, JC Hanson, CP Grey. Micropor Mesopor Mater 49:111, 2001.
129. LW Beck, JL White, JM Haw. J Am Chem Soc 116:9657, 1994.
130. Z Luz, AJ Vega. J Phys Chem 91:365 1987.
131. JL White, LW Bechk, JF Haw. J Am Chem Soc 114:6182, 1992.
132. JF Haw, JB Nicholas, T Xu, LW Beck, DB Ferguson. J Am Chem Soc 29:259, 1996.
133. JF Haw, T Xu, JB Nicholas, PW Goguen. Nature 389:832, 1997.
134. RJ Gorte, D White. Top Catal 4:57, 1997.
135. F Haase, J Sauer. J Phys Chem 98:3083, 1994.
136. D Michel, A Germanus, H Pfeifer. J Chem Soc, Faraday Trans 1 78:237, 1982.
137. WP Rothwell, W Shen, JH Lunsford. J Am Chem Soc 106:2452, 1984.
138. D Farcasiu, R Leu, A Corma. J Phys Chem B 106:928, 2002.
139. GE Maciel, JF Haw, IS Chuang, BL Hawkins, TA Early, DR McKay, L Petrakis. J Am Chem Soc 105:5529, 1983.
140. JH Lunsford, WP Rothwell, W Shen. J Am Chem Soc 107:1540, 1985.
141. JF Haw, IS Chuang, BL Hawkins, GE Maciel. J Am Chem Soc 105:7206, 1983.
142. A Corma. Chem Rev 95:559, 1995.
143. WE Farneth, RJ Gorte. Chem Rev 95:615, 1995.
144. EF Rakiewicz, AW Peters, RF Wormsbecher, SK J., KT Mueller. J Phys Chem B 102:2890, 1998.
145. AI Biaglow, RJ Gorte, D White. J Phys Chem 97:7135, 1993.
146. AI Biaglow, RJ Gorte, GT Kokotailo, D White. J Catal 148:779, 1994.
147. MD Karra, KJ Sutovich, KT Mueller. J Am Chem Soc 124:902, 2002.
148. AL Blumenfeld, JJ Fripiat. J Phys Chem B 101:6670, 1997.
149. D Coster, A Blumenfeld, JJ Fripiat. J Phys Chem 98:6201, 1994.
150. CP Grey, B. S. A. Kumar. J Am Chem Soc 117:9071, 1995.
151. H-M Kao, H Liu, JC Jiang, S-H Lin, CP Grey. J Phys Chem B 104:4923, 2000.
152. EJ Teunissen, RA van Santen, AP Jansen, FB van Duijneveldt. J Phys Chem 97:203, 1993.
153. EH Teunissen, FB van Duijnevedlt, RA van Santen. J Phys Chem 96:366, 1992.
154. HM Kao, CP Grey. J Am Chem Soc 119:627, 1997.
155. B Zhao, H Pan, JH Lunsford. Langmuir 15:2761, 1997.
156. A Bendada, E DeRose, JJ Fripiat. J Phys Chem 98:3838, 1994.
157. A Lewis, PhD thesis, University of British Columbia, 1998.
158. E Bosch, S Huber, J Weitkamp, H Knozinger. Phys Chem Chem Phys 1:579, 1999.
159. M Sanchez-Sanchez, T Blasco. Chem Commun 491, 2000.
160. MF Ciraolo, JC Hanson, BH Toby, CP Grey. J Phys Chem B 105:12330, 2001.
161. M Sanchez-Sanchez, T Blasco, F Rey. Phys Chem Chem Phys 1:4529, 1999.
162. V Bosacek. J Phys Chem 97:10732, 1993.
163. V Bosacek, H Ernst, D Freude, T Mildner. Zeolites 18:196, 1997.
164. V Bosacek, R Klik, F Genoni, G Spano, F Rivetti, F Figueras. Magn Reson Chem 37:S135, 1999.
165. U Schenk, M Hunger, J Weitkamp. Magn Reson Chem 37:S75, 1999.
166. DK Murray, T Howard, PW Goguen, TR Krawietz, JF Haw. J Am Chem Soc 116:6354, 1994.
167. DK Murray, JW Chang, JF Haw. J Am Chem Soc 115:4732, 1993.
168. KH Lim, F Jousse, SM Auerbach, CP Grey. J Phys Chem B 105:9918, 2001.
169. MW Anderson, J Klinowski. Nature 339:200, 1989.
170. TA Carpenter, J Klinowski, DTB Tennakoon, CJ Smith, DC Edwards. J Magn Reson 68:561, 1986.
171. H Liu, H-M Kao, CP Grey. J Phys Chem B 103:4786, 1999.
172. H Ernst, D Freude, T Mildner, I Wolf. Solid State NMR 6:147, 1996.

173. T Mildner, H Ernst, D Freude, WF Holderich. J Am Chem Soc 119:4258, 1997.
174. P Sarv, T Tuherm, E Lippmaa, K Keskinen, A Root. J Phys Chem 99:13763, 1995.
175. T Mildner, D Freude. J Catal 178:309, 1998.
176. T Mildner, H Ernst, D Freude, J Karger, U Winkler. Magn Reson Chem 37:S38, 1999.
177. JF Haw, PW Goguen, T Xu, TW Skloss, W Song, Z Wang. Angew Chem Int Ed 37:948, 1998.
178. M Hunger, M Seiler, T Horvath. Catal Lett 57:199, 1999.
179. M Hunger, M Seiler, A Buchholz. Catal Lett 74:61, 2001.
180. M Seiler, W Wang, M Hunger. J Phys Chem B 105:8143, 2001.
181. W Wang, M Seiler, M Hunger. J Phys Chem B 105:12553, 2001.
182. W Wang, M Seiler, Ivanova, II, J Weitkamp, M Hunger. Chem Commun 1362, 2001.
183. AJ Vega, Quadrupolar nuclei in solids. In: Encyclopedia of NMR, DM Grant, RK Harris, eds. Chichester, UK: Wiley, 1996, p 3869.
184. J Skibstedt, NC Nielsen, H Bildsoe, HJ Jacobsen. J Magn Reson 95:88, 1991.
185. C Jäger. In: NMR Basic Principles and Progress. Berlin: Springer-Verlag, 1994, Vol. 31, p 133.
186. D Müller. Ann Phys (Leipzig) 39:451, 1982.
187. A Samoson, E Lippmaa. J Magn Reson 84:410, 1989.
188. S Vega, Y Naor. J Chem Phys 75:75, 1981.
189. PJ Grandinetti, JH Baltisberger, A Llor, YK Lee, U Werner, MA Eastman, A Pines. J Magn Reson 103:72, 1993.
190. SP Brown, S Wimperis. J Magn Reson 128:42, 1997.
191. JP Amoureux, C Fernandez, S Steuernagel. J Magn Reson A123:116, 1996.
192. D Massiot. J Magn Reson A 122:240, 1996.
193. PK Madhu, A Goldbourt, L Frydman, S Vega. Chem Phys Lett 307:41, 1999.
194. PK Madhu, A Goldbourt, L Frydman, S Vega. J Chem Phys 112:2377, 2000.
195. APM Kentgens, D Iuga, M Kalwei, H Koller. J Am Chem Soc 123:2925, 2001.
196. APM Kentgens, R Verhagen. Chem Phys Lett 300:435, 1999.
197. M Pruski, JW Wiench, JP Amoureux. J Magn Reson 147:286, 2000.
198. P Zhao, PS Neuhoff, JF Stebbins. Chem Phys Lett 344:325, 2001.
199. NC Nielsen, H Bildsoe, HJ Jakobsen. Chem Phys Lett 191:205, 1992.
200. A Samoson, E Lippmaa. Chem Phys Lett 100:205, 1983.
201. APM Kentgens, JJM Lemmens, FMM Geurts, WS Veeman. J Magn Reson 71:62, 1987.
202. GAH Tijink, R Janssen, WS Veeman. J Am Chem Soc 109:7301, 1987.
203. G Engelhardt, M Hunger, H Koller, J Weitkamp. In: Exploring Cation Siting in Zeolites By Solid-State NMR of Quadrupolar Nuclei. Studies in Surface Science and Catalysis. Amsterdam: Elsevier Science, 1994, Vol. 84, p 421.
204. D Massiot, C Bessada, JP Coutures, F Taulelle. J Magn Reson 90:231, 1990.
205. AJ Vega. J Magn Reson 96:50, 1992.
206. AJ Vega. Solid State NMR 1:17, 1992.
207. Y Wu, D Lewis, JS Frye, AR Palmer, RA Wind. J Magn Reson 100:425, 1992.
208. Y Ba, HM Kao, CP Grey, L Chopin, T Gullion. J Magn Reson 133:313, 1998.
209. PJ Chu, RR Carvajal, JH Lunsford. Chem Phys Lett 175:407, 1990.
210. B Herzog, EL Hahn. Phys Rev 103:148, 1956.
211. T Gullion, J Schaefer. J Magn Reson 81:196, 1989.
212. T Gullion. Concepts Magn Reson 10:277, 1998.
213. AW Hing, S Vega, J Schaefer. J Magn Reson 96:205, 1992.
214. J Klinowski, S Ramdas, JM Thomas, CA Fyfe, JS Hartmann. J Chem Soc, Faraday Trans 2:1025, 1982.
215. DF Shantz, RF Lobo. J Phys Chem B 102:2339, 1998.
216. I Kustanovich, Z Luz, S Vega, AJ Vega. J Phys Chem 94:3138, 1990.
217. I Kustanovich, HM Vieth, Z Luz, S Vega. J Phys Chem 93:7427, 1989.
218. M Haouas, C Gerardin, F Taulelle, C Estournes, T Loiseau, G Ferey. J Chim Phys Phys Chim Biol 95:302, 1998.

219. C Gerardin, M In, L Allouche, M Haouas, F Taulelle. Chem Mater 11:1285, 1999.
220. H Nakayama, DD Klug, CI Ratcliffe, JA Ripmeester. J Am Chem Soc 116:9777, 1994.
221. VI Srdanov, GD Stucky, E Lippmaa, G Engelhardt. Phys Rev Lett 80:2449, 1998.
222. KL Moran, PD Barker, JE Readman, PP Edwards, R Dupree, PA Anderson. Chem Commun 55, 1999.
223. G Engelhardt, M Feuerstein, P Sieger, D Markgraber, G Stucky, V Srdanov. Chem Commun 729, 1996.
224. HK Kira, H Tou, Y Maniwa, Y Murakami. J Magnetism Mag Mater 3002:1095, 2001.
225. I Heinmaa, S Vija, E Lippmaa. Chem Phys Lett 131, 2000.
226. A Eldewik, JM Hook, NK Singh, RF Howe. Magn Reson Chem 37:S63, 1999.
227. T Baba, N Komatsu, H Sawada, Y Yamaguchi, T Takahashi, H Sugisawa, Y Ono. Langmuir 15:7894, 1999.
228. VV Terskikh, IL Moudrakovski, HB Du, CI Ratcliffe, JA Ripmeester. J Am Chem Soc 123:10399, 2001.
229. CJ Jameson, AC de Dios. J Chem Phys 116:3805, 2002.
230. RG Larsen, J Shore, K Schmidt Rohr, L Emsley, H Long, A Pines, M Janicke, BF Chmelka. Chem Phys Lett 214:220, 1993.
231. SL Burkett, ME Davis. J Phys Chem 98:4647, 1994.
232. SL Burkett, ME Davis. Chem Mater 7:920, 1995.
233. L van Wullen, M Kalwei. J Magn Reson 139:250, 1999.
234. WPJH Jacobs, JW de Haan, LJM van de Ven, RA van Santen. J Phys Chem 97:10394, 1993.
235. D Freude, T Frohlich, M Hunger, H Pfeifer, G Scheler. Chem Phys Lett 98:263, 1983.
236. D Freude, J Klinowski, H Hamdan. Chem Phys Lett 49:355, 1988.